Department of Micro- and Nanosciences

Silver nanoparticles embedded in glass by ion exchange method for biosensor applications

Ya Chen

Aalto University

DOCTORAL DISSERTATIONS

Aalto University publication series
DOCTORAL DISSERTATIONS 125/2012

Silver nanoparticles embedded in glass by ion exchange method for biosensor applications

Ya Chen

A doctoral dissertation completed for the degree of Doctor of Science (Technology) (Doctor of Philosophy) to be defended, with the permission of the Aalto University School of Electrical Engineering, at a public examination held at the lecture hall T2 of the Computer Science Building (Konemiehentie 2, Espoo, Finland) on the 26th of October 2012 at 12 noon.

Aalto University
School of Electrical Engineering
Department of Micro- and Nanosciences
Photonics group

Supervising professor
Prof. Seppo Honkanen

Thesis advisor
Doc. Ari Tervonen

Preliminary examiners
Prof. Tapio Niemi, Tampere University of Technology, Finland
Prof. Brian West, Wilfrid Laurier University, Canada

Opponent
Dr. Gualtiero Nunzi Conti, Institute of Applied Physics "Nello Carrara", Italy

Aalto University publication series
DOCTORAL DISSERTATIONS 125/2012

ISBN 978-952-60-4801-7 (printed)
ISBN 978-952-60-4802-4 (pdf)
ISSN-L 1799-4934
ISSN 1799-4934 (printed)
ISSN 1799-4942 (pdf)
http://urn.fi/URN:ISBN:978-952-60-4802-4

Unigrafia Oy
Helsinki 2012

Finland

441 697
Printed matter

Author
Ya Chen

Name of the doctoral dissertation
Silver nanoparticles embedded in glass by ion exchange method for biosensor applications

Publisher School of Electrical Engineering

Unit Department of Micro- and Nanosciences

Series Aalto University publication series DOCTORAL DISSERTATIONS 125/2012

Field of research Photonics

Manuscript submitted 1 June 2011 **Date of the defence** 26 October 2012

Permission to publish granted (date) 23 September 2012 **Language** English

☐ **Monograph** ☒ **Article dissertation (summary + original articles)**

Abstract

This thesis focuses on the fabrication of silver nanoparticles (Ag NPs) embedded in glasses and their applications for surface enhanced Raman spectroscopy (SERS).

Firstly, Ag NPs are produced in microscope slides and high iron float glasses by ion exchange with thermal treatment. These two kinds of glasses contain a different percentage of iron oxide, which acts as the reducing agent in a silver reduction process. The study shows that the iron content in the Fe2+ form is more important than that in the Fe3+ form for the silver reduction. It is also demonstrated that Ag NP aggregates embedded in high iron float glasses can make them as SERS-active substrates.

Secondly, Ag NPs are formed in high quality Corning 0211 glasses by a masked ion exchange and a two-step ion exchange. Ag NPs are deposited just under the mask edge due to the electrolytic deposition taking place in the masked ion exchange process. They form into Ag NP patterns according to the mask pattern. With the two-step ion exchange, uniform nanoparticle clusters over large areas are embedded in glass due to the galvanic replacement reaction and the electrolytic deposition. When applying a photolithographic mask in either the first step of an Ag+ ion exchange or the second step of a K+ ion exchange process, the two-step ion exchange can also enable the patterning of areas with particles having desired shapes and sizes. The SERS performance of the particles formed by these two methods is also demonstrated.

The presented methods based on ion exchange are simple and potentially low-cost processes for large scale fabrication of SERS-active substrates. Furthermore, the two methods used to fabricate Ag NPs in the high quality Corning 0211 glass are ideal options in the development of integrated sensor chips by combining optical waveguides and microfluidics with the formed nanoparticles.

Keywords silver nanoparticles, ion exchange, surface enhanced Raman scattering

ISBN (printed) 978-952-60-4801-7 **ISBN (pdf)** 978-952-60-4802-4

ISSN-L 1799-4934 **ISSN (printed)** 1799-4934 **ISSN (pdf)** 1799-4942

Location of publisher Espoo **Location of printing** Helsinki **Year** 2012

Pages 131 **urn** http://urn.fi/URN:ISBN:978-952-60-4802-4

Preface

The research presented in this thesis has been performed in the Photonics Group of the Department of Micro and Nanosciences at Aalto University. The Academy of Finland is acknowledged for funding the work.

My deepest gratitude goes to my supervisor, Professor Seppo Honkanen, for introducing me to the fascinating "nano" world, offering the great work opportunity and the sparkling ideas, and providing his endless help to my study and to my life. I am also very grateful to my instructor, Doc. Ari Tervonen, for his fruitful discussions and invaluable suggestions on the work, particularly on the publications and the thesis. Professor Harri Lipsanen is also appreciated for providing the enjoyable atmosphere in our department and offering his help in the last stages of my study.

Dr. Antti Säynätjoki is acknowledged for his patient guidance, efficient discussions and also important comments on the publications. I am particularly thankful to the co-workers of this work, Janne Jaakola and Lasse Karvonen, for their important input in the work and for their sharing about travel, life and everything. I also thank the other people in our group: Dr. Changgeng Ye, Dr. Mikko Söderlund, Dr. Tapani Alasaarela, Amit Khanna, Joan Jesus Montiel i Ponsoda, Shuo Li and Aarni Iho. It has been my precious experience to work with such great colleagues.

In addition, many great people whom I have worked with are acknowledged, especially Dr. Tommy Holmqvist, Dr. Matthias Meschke, Dr. Nikolai Chekurov, Wonjae Kim, and Pasi Kostamo, for sharing their valuable knowledge and for forgiving many of my stupid questions. I wish to thank Dr. Yanling Ge, Dr. Hua Jiang and Zhen Zhu for providing their help in TEM observations and analysis, and Dr. Sami Kujala for the interesting discussions about Mie's theory.

Furthermore, I would like to thank the pre-examiners of the thesis, Prof. Brian West and Prof. Tapio Niemi. Their critical review and suggestions were important for the improvements of the thesis.

Finally, I want to thank my family and my friends for sharing every

wonderful moment during the years. Especially, I express my warmest gratitude to my parents for their encouragement and assistance, to my husband / colleague Dr. Changgeng Ye for his continuous love and support and also for his contribution to my research, and to my little boy Tianhao for giving me the sweetest smiles.

Espoo, September 25, 2012,

Ya Chen

Contents

List of Publications

This thesis consists of an overview and of the following publications which are referred to in the text by their Roman numerals.

I Y. Chen, J. Jaakola, Y.L. Ge, A. Säynätjoki, A. Tervonen, S.-P. Hannula and S. Honkanen. In situ fabrication of waveguide-compatible glass-embedded silver nanoparticle patterns by masked ion-exchange process. *J. Non-Cryst. Solids*, 355, 45-47, 2224–2227, 2009.

II Y. Chen, J. Jaakola, A. Säynätjoki, A. Tervonen, and S. Honkanen. SERS-active silver nanoparticles in ion-exchanged glass. *J. Nonlinear Opt. Phys. Mater.*, 19, 4, 527–533, 2010.

III Y. Chen, J. Jaakola, A. Säynätjoki, A. Tervonen, and S. Honkanen. Glass-embedded silver nanoparticle patterns by masked ion-exchange process for surface-enhanced Raman scattering. *J. Raman Spectrosc.*, 42, 5, 936–940, 2011.

IV Y. Chen, L. Karvonen, A. Säynätjoki, C.G. Ye, A. Tervonen, and S. Honkanen. Ag nanoparticles embedded in glass by two-step ion exchange and their SERS application. *Opt. Mater. Express*, 1, 2, 164–172, 2011.

V L. Karvonen, Y. Chen, A. Säynätjoki, A. Tervonen, and S. Honkanen. SERS-active silver nanoparticle aggregates produced in high-iron float glass by ion exchange process. *Opt. Mater.*, 34, 1, 1–5, 2011.

Author's Contribution

Publication I: "In situ fabrication of waveguide-compatible glass-embedded silver nanoparticle patterns by masked ion-exchange process"

The author did most of the experiments and prepared the manuscript. The TEM characterizations were done in collaboration with the Department of Materials Science and Engineering, Aalto University.

Publication II: "SERS-active silver nanoparticles in ion-exchanged glass"

The author did the experiments related to the masked ion exchange method, participated in the experiments related to the ion exchange with the thermal treatment method, and contributed in writing of the manuscript.

Publication III: "Glass-embedded silver nanoparticle patterns by masked ion-exchange process for surface-enhanced Raman scattering"

The author did most of the experiments and prepared the manuscript.

Publication IV: "Ag nanoparticles embedded in glass by two-step ion exchange and their SERS application"

The author did the experiments except the TEM observation, carried out the data analysis, and prepared the manuscript.

Publication V: "SERS-active silver nanoparticle aggregates produced in high-iron float glass by ion exchange process"

The author participated in the experiments and in the preparation of the manuscript.

1 Introduction

Stained glass with beautiful colors has been used a lot as the windows of churches since ancient times. The intense scattering and absorption of the light by noble metal nanoparticles is the source of glass tinting and coloration. The nature of this phenomenon, attributed to the light interaction with metallic nanoparticles, has attracted continuous interest of scientists for years. Mie's scattering theory is the first work to give the theoretical analysis for the optical properties of spherical metal nanoparticles [1]. Surface plasmons, particularly localized surface plasmons in the case of metal nanoparticles, explain the properties from the viewpoint of physical phenomenon and present the changes of the electromagnetic field due to the presence of metal particles [2–4]. In recent years, plasmonics as a subfield of nanophotonics has appeared and developed rapidly. It primarily focuses on the plasmon coupling effects within close proximity along metal nanostructures and on the manipulation of light at the nanoscale based on the properties of propagating and localized surface plasmons [5, 6]. Two promising applications for plasmonics include [7]: i) plasmonic waveguides to guide electromagnetic energy below the diffraction limit along for example continuous metal strips or the chains of closely spaced metal nanoparticles, and ii) plasmonic sensors to realize various types of sensing schemes based on surface plasmon resonances, such as refractive-index plasmon sensing [8], surface enhanced Raman spectroscopy (SERS) [9], and metal enhanced fluorescence [10].

In the biosensing field of metal nanoparticles, SERS is one of the most important applications, because it significantly increases the feasibility of many detection techniques by greatly enhancing the detected signal [11–15]. SERS, discovered by Fleischmann et al. in 1974 [16], is currently experiencing a growing interest due to the important discovery of the single molecule SERS (SMSERS) [17, 18] and the explosion of the research in plasmonics [19, 20]. Conventional SERS, whose intensity exceeds that of the normal Raman spectrum by a factor of 10^8 - 10^{10}, is attributed to two

main contributors: i) the conventional electromagnetic enhancement as a result of a localized surface plasmon resonance and ii) the chemical enhancement brought out by a charge transfer process between the analyte molecules and the metal nanoparticles [21, 22]. For the extremely high enhancement in SMSERS, near-field dipole interaction occurring within the narrow gap between the closely packed particles is explained as the main reason, and the long-range interaction in periodic arrays of particles could be an additional contributor [23, 24]. For the random metal nanostructures, a self-similar system containing particles of different sizes in a chain, which is supposed to work like a nanolens to focus and concentrate the optical energy into a small area, has been proposed [9, 20].

Besides the explanation of the SERS mechanism, various SERS-active substrates have been developed for practical SERS applications. With the development of nanofabrication, metal nanoparticles can be produced on the substrates by many kinds of techniques, making the substrates SERS-active. Electron beam lithography [25, 26], DUV photolithography [27], modified on-wire lithography [28] and focused ion beam patterning [29] are ideal options to investigate the SERS mechanism, because they can be used to precisely control the size and spacing of the nanostructures. Some other methods, such as Langmuir-Blodgett technique [30, 31], chemical reduction process [32, 33], self-assembled synthesis [34], ion exchange with some additional processing [35] and so on, are employed to fabricate random metal nanostructures. In these disordered nanostructures, such as fractal aggregates of silver or gold, extremely high SERS enhancement is often observed on some so-called "hot spot" sites. Recently, metal nanoparticles combined with carbon nanotubes [36], polymers [37] and some other materials [38, 39], have also been explored. The high sensitivity, reproducibility, and stability are the important criteria required from the SERS-active substrates. In order to realize a remote or an easy Raman measurement, the capability of integration with other components, such as optical waveguides and microfluidic channels, is also of interest.

In this work, three different methods based on ion exchange have been developed and utilized to fabricate Ag nanoparticles, namely an ion exchange with thermal treatment, a masked ion exchange and a two-step ion exchange. The properties of the nanoparticles are studied by several characterization techniques and the formation mechanisms in these three methods are discussed. Finally, SERS activities of the particles are demonstrated and compared by using rhodamine 6G as an analyte.

The thesis is organized as follows. Chapter 2 introduces some fundamental concepts and basic theories relevant to this thesis. Chapter 3 and 4 describe the materials and methods of the experiments and the characterization tools utilized in this work. Chapter 5 presents the properties and the SERS applications of the Ag nanoparticle aggregates formed in microscope slides and high iron float glasses. The mechanism of how these aggregates are formed is also discussed. Chapter 6 presents the studies of Ag nanoparticle patterns made by the masked ion exchange. The localized electrolytic deposition is presented as the formation mechanism. Chapter 7 presents a fully covered SERS-active substrate made by the two-step ion exchange. The properties of the substrate are studied and the formation mechanism is explained by a combination effect of a galvanic replacement reaction and an electrolytic deposition. Finally, some conclusions are drawn and the outlook of this work is discussed.

2 Background

2.1 Optical properties of metal nanoparticles

People knew how to utilize metal particles before discovering them. In ancient Rome, they made small colored glass objects with gold or silver particles. The famous one is the Lycurgus Cup (Fig. 2.1), which is made of ruby glass. When viewed in reflected light, for example in daylight, it appears green. However, when light is shone into the cup and transmitted through the glass, it appears red. After that, in middle ages, stained glass windows were popular in Europe. Even today, you can see them in many famous cathedrals and churches.

Figure 2.1: The Lycurgus Cup [40].

In 1857, Michael Faraday discovered the optical properties of gold colloids and theorized that coloration was due to finely divided gold particles [41]. In 1908, Mie's theory represented the first rigorous theoretical treatment of the optical properties of spherical metal particles with a diameter $d \ll \lambda$, where λ is the wavelength of light in the surrounding medium. His scattering theory is still used today, even for nonmetal particles [1]. From that on, more and more researchers paid their attention to metal particles, including their optical, electrical and chemical properties, and developed various applications in different fields. The interaction of light

with noble metal nanoparticles has been a significant founding for scientific research.

2.1.1 Localized surface plasmon by a single particle

A surface plasmon is a collective oscillation of the free electron gas that exists at the interface between two materials, normally a metal / dielectric interface. When a surface plasmon is resonant with incident light on a flat metal / dielectric interface, it results in a surface plasmon polariton appearing as an electromagnetic field confined at the metallic surface, a so-called propagating surface plasmon. On the other hand, if the collective oscillation of the conduction electrons is resonant with the incident photon frequency, and limited in a small volume such as a metal nanoparticle, it is known as a localized surface plasmon. A strongly enhanced optical field is spatially confined in the particle location, and it oscillates in time with the frequency of the incident light.

The localized surface plasmon plays an important role in the optical properties of metal nanoparticles. As shown in Fig. 2.2, when the metal particles are excited by the light, the free electrons in the particles can be driven by the electric field of the applied light. The conduction electrons and lattice ions will be placed on the opposite sites of the particles. Those charges attract each other by a restoring force, resulting in a resonance to occur at a specific frequency dependent on the composition, size and shape of the metal particles and also on the surrounding dielectric material [2, 9].

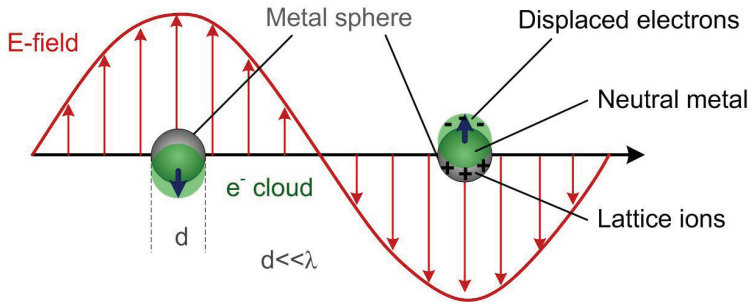

Figure 2.2: The schematic of a surface plasmon oscillation for a spherical metal nanoparticle.

Due to the localized surface plasmon resonance, optical properties of metal nanoparticles, especially those of noble metals, show striking dif-

ferences compared with optical responses of the same materials in bulk or thin film form. Generally, optical properties of metal nanoparticles are expressed in terms of absorption and scattering cross sections σ_{abs} and σ_{sca}, and the resulting extinction cross section is given by the sum of them:

$$\sigma_{ext} = \sigma_{abs} + \sigma_{sca}.$$

When the size of a spherical particle is much smaller than the wavelength of light ($d \ll \lambda$), the electric field of the light can be assumed to be constant, and the interaction between the nanoparticles and the incident light is governed by electrostatics rather than electrodynamics. Phase retardation and effects of higher multipoles are neglected. This is a so-called quasistatic approximation. By solving LaPlace's equation $\nabla^2\Phi = 0$, where Φ is the electric potential, with appropriate boundary conditions at the sphere surface, the electric potential can obtained to determine the field outside the sphere E_{out}, which includes the applied field and the induced dipole field. The corresponding static electric polarizability of the sphere derived from the induced dipole field is:

$$\alpha = 4\pi a^3 \frac{\epsilon - \epsilon_m}{\epsilon + 2\epsilon_m},$$

where ϵ_m is the dielectric function of the embedding medium, a is the radius of the particle, and ϵ, a function of frequency ω, is the complex dielectric function of the particle material with the real and imaginary parts $\epsilon(\omega) = \epsilon_1(\omega) + i\epsilon_2(\omega)$. The cross sections for scattering and absorption σ_{sca} and σ_{abs} can be calculated as:

$$\sigma_{sca} = \frac{8\pi}{3} k^4 a^6 \left| \frac{\epsilon - \epsilon_m}{\epsilon + 2\epsilon_m} \right|^2,$$

$$\sigma_{abs} = 4\pi k a^3 Im \left[\frac{\epsilon - \epsilon_m}{\epsilon + 2\epsilon_m} \right].$$

For a small sphere ($d \ll \lambda$) in the quasistatic regime, the extinction cross section is only due to a dipole absorption since the scattering cross section is scaling with a^6 and strongly suppressed. The explicit expression for the extinction cross section is simplified considerably as:

$$\sigma_{ext}(\omega) = 9\frac{\omega}{c}\epsilon_m^{3/2} V_0 \frac{\epsilon_2(\omega)}{[\epsilon_1(\omega) + 2\epsilon_m]^2 + \epsilon_2(\omega)^2},$$

where $V_0 = (4\pi/3)a^3$ denotes the particle volume. The equation shows that the cross section is dependent on the material $(\epsilon(\omega))$ and the size (V_0) of the particle, and its dielectric environment (ϵ_m). It experiences a resonant enhancement when the Frölich condition $\epsilon_1(\omega) = -2\epsilon_m$ is satisfied.

In the Lorentz-Drude model, $\epsilon(\omega)$ can be written as:

$$\epsilon(\omega) = 1 - \frac{\omega_p^2}{\omega^2 + i\Gamma\omega} = 1 - \frac{\omega_p^2}{\omega^2 + i\Gamma^2} + i\frac{\omega_p^2\Gamma}{\omega(\omega^2 + \Gamma^2)},$$

where ω equals the frequency of the surface plasmon oscillation, ω_p is the Drude plasma frequency and Γ denotes the relaxation constant. In particular, for free electron metals with $\omega \gg \Gamma$,

$$\epsilon_1(\omega) \approx 1 - \frac{\omega_p^2}{\omega^2},$$

$$\epsilon_2(\omega) \approx \frac{\omega_p^2}{\omega^3}\Gamma.$$

By inserting $\epsilon_1(\omega)$ and $\epsilon_2(\omega)$ in the explicit expression for the extinction cross section, in the vicinity of the resonance, the lineshape of the extinction cross section is described by a Lorentzian:

$$\sigma_{ext}(\omega) = \sigma_0 \frac{1}{(\omega - \omega_1)^2 + (\Gamma/2)^2}.$$

The resonance position can be calculated from the plasma frequency of the respective metal:

$$\omega_1 = \omega_p/\sqrt{1 + 2\epsilon_m}.$$

The above calculation is derived for a single sphere and is strictly valid only in the limit of vanishingly small particles [2, 42, 43]. For particles of larger dimensions, a complete theory was developed by Mie in 1908, by solving Maxwell's equations for the scattering and absorption of electromagnetic radiation by a spheroidal or an ellipsoidal object [1]. The above quasistatic results, valid for sub-wavelength spheres, are then recovered by a power series expansion of the absorption and scattering coefficients and retaining only the lowest order term. For more complex shapes, some advanced numerical methods such as the T-matrix method [44], the discrete dipole approximation [45] or finite difference time domain simulations [46] are employed to determine the resonance frequencies and also the local electric field in the vicinity of the particles.

2.1.2 Coupling effect in particle ensembles

With the development of nanofabrication techniques, such as focused ion beam [29] and electron beam lithography [26, 47], researchers are able to have more control on the size and the distribution of metal nanoparticles. In particle ensembles, additional influences on the optical property

of particles occur due to the interaction between particles. From the viewpoint of the electromagnetic theory, the particles with a diameter d, much smaller than the wavelength λ of the exciting light, act as the electric dipoles, and the particle ensembles can be treated as the ensembles of interacting dipoles.

When the spacing between particles d_c is much smaller than the wavelength of light λ, the ensembles appear as closely packed particles, which can be described as an array of point dipoles interacting via their near-field. This near-field dipolar interaction between adjacent particles is highly distance-dependent with a distance dependence of d_c^{-3}. A strong field localization is caused by a suppression of scattering into the far-field [48]. For a larger spacing (d_c is comparable with λ), far-field dipolar interaction with a distance dependence of d_c^{-1} dominates. The ensemble can then be treated as a grating, and it has a coupling effect via diffraction [49].

2.2 Surface enhanced Raman spectroscopy

Plasmonic biosensing deals with a broad range of applicability of using surface plasmon waves. The simplest and most popular biosensing application is refractive-index plasmon sensing, which has been widely used to monitor the analyte-surface binding interactions. It utilizes the evanescent field of a special mode of an electromagnetic field - the surface plasmon - to measure the change of refractive index that occurs in response to the analyte binding at or near a metal surface [4]. Propagating and localized surface plasmon resonances (SPR) are both utilized in this application - the propagating SPR at flat metal / dielectric boundaries with metal strips and nanowires, and the localized SPR around metal nanoparticle structures [2, 50–52]. Another important application, which is utilized as the characterization method in this work, is the surface enhanced Raman scattering (SERS) [51, 53, 54]. Both periodic and random metal nanostructures are fabricated to enhance local electromagnetic fields near the surface of the structures and to obtain an intense Raman signal. In addition, the mechanism in surface-enhanced fluorescence is analogous to that in SERS, by utilizing the enhanced local electromagnetic fields near the surface of the nanoparticle to increase the final quantum yield [10].

2.2.1 Surface enhanced Raman scattering

Raman scattering is inelastic scattering of a photon. When the energy of the incident light is not large enough to excite a molecule from the ground state to the lowest electronic state, the molecule will be excited to a virtual state between the two states. If the molecule returns to its original ground state with no energy exchange between the incident light and the molecule, the frequency of the scattered light is the same as that of the light source. This process is called Rayleigh scattering. It is also possible that the molecule returns to a vibrational state different from its original state, thus there is an energy difference between the emitted photon and the incident photon. For the energy conservation, optical phonon is involved, carrying the energy of the molecular vibration which corresponds to the energy difference of the two photons. If the frequency of the emitted photon is smaller than that of the incident photon, the process is called the Stokes scattering. The opposite is called the anti-Stokes scattering. Their frequencies are symmetrical on the both sides of the Rayleigh scattering as the centre point in spectrum. The quantum illustration for different cases of scattering is shown in Fig. 2.3.

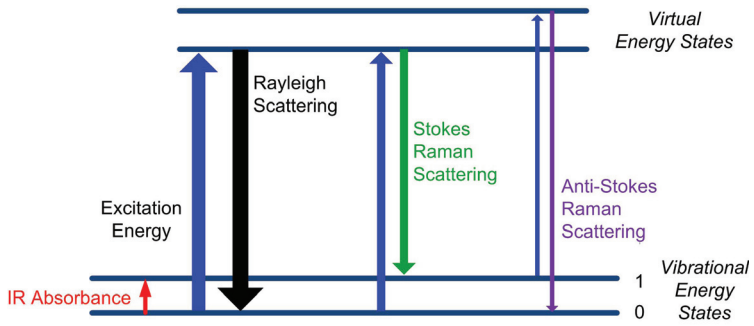

Figure 2.3: The quantum illustration for different cases of scattering.

Raman spectroscopy is used to analyze materials. The frequency of light changes in Raman scattering, and the frequency shift depends on the property of the material. Researchers have tried to use Raman spectroscopy to detect molecules, but it is quite difficult because of the disadvantage of the small cross section of Raman scattering.

Surface enhanced Raman spectroscopy (SERS) was discovered, though not recognized as such, by Fleischmann et al. in 1974, who observed intense Raman scattering from pyridine adsorbed onto a roughened silver

electrode surface from aqueous solution [16]. This enormously strong signal enhanced by a factor of 10^4-10^6, had much higher intensity compared to the ordinary Raman scattering, and was debuted as surface enhanced Raman scattering. In 1977, two groups independently proposed a mechanism for the observed enhancement. Jeanmaire and Van Duyne proposed an electromagnetic effect [55], while Albrecht and Creighton proposed a charge-transfer effect [56]. M. Moskovits summarized these two effects in a conventional SERS enhancement in 1985 [21]. The typical SERS-active substrates include nanoparticle aggregates, rough metal surfaces, and islands on the film. Silver is widely used in SERS sensors, but one issue is that silver is easily oxidized. Recently, atomic layer deposition (ALD) has been employed to deposit an ultrathin layer of Al_2O_3 to protect the silver surface and thus improve the stability of the substrates [57, 58]. The most popular materials of SERS-active sites are silver and gold, but copper is also of interest because of its abundant presence on the earth [59]. Various factors including material, size, shape, dielectric environment and arrangement can give an influence to the SERS activity.

Single molecule SERS (SMSERS) was originally developed independently by Nie and Emory [17] and Kneipp [18] et al. in 1997, exhibiting a nominal enhancement factor larger than 10^{13}. They proposed that the "hot spots", which are defined as nanostructures consisting of two or more coupled nanoparticles or nanostructured surfaces with closely spaced features, provide the high enhancement. This significant discovery, together with the developments in nanophotonics and plasmonics, has generated a growing interest in SERS [19, 20].

2.2.2 SERS-active substrates and enhancement mechanism

Generally, the total enhancement in SERS is a product of two mechanisms: i) the electromagnetic enhancement [21] and ii) the chemical enhancement [22].

Conventional electromagnetic enhancement

In the well-known electromagnetic enhancement mechanism, the field enhancement is the ratio of the field at the position of the SERS-active site and the incoming field. It can be expressed by $g(\omega) = |E_{loc}(\omega)| \,/\, |E_0|$, where $|E_{loc}(\omega)|$ is the amplitude of the local field at the SERS-active site, and $|E_0|$ is the field of the incident light. The total enhancement factor G is

given by $G = |g(\omega)|^2 |g(\omega')|^2$, where $g(\omega)$ is the local electric field enhancement factor at the incident frequency ω, and $g(\omega')$ is the corresponding factor at the Stokes-shifted frequency ω'. Since the Stokes frequency shift $\Delta\omega = \omega - \omega'$ is in general much smaller than the plasmon bandwidth, the electromagnetic contribution to the total SERS enhancement $G = |g(\omega)|^4$ by assuming that $g(\omega)$ and $g(\omega')$ are the same.

For some simple geometries, in order to obtain G, two physical phenomena should be considered as the main contributions to the enhancement in the conventional electromagnetic enhancement mechanism. The first one is the enhancement due to the resonant excitation of localized surface plasmons in metallic nanostructures. Localized surface plasmons have the ability to strongly scatter and absorb light and to generate an inhomogeneous distribution of intense light highly localized into nanometer dimensions, which can produce a large enhancement of local electromagnetic fields. It has been considered as a conventional SERS enhancement, and the rigorous expression has been obtained for some simple structures such as spherical or ellipsoidal particles. The second one is a so-called lightening rod effect, which is due to a crowding of the electric field lines. The accompanying enhancement at the metal surface is caused purely by geometries, such as sharp metallic tips. However, the highest SERS enhancement, SMSERS for example, often happens at some more complex geometries rather than a single simple object, which cannot be simply explained by the conventional electromagnetic enhancement.

Coupling effects

For SERS at complex geometries, the plasmon coupling effect is involved, and in general more advanced numerical calculation methods are employed to obtain the enhancement factor. For example, the finite difference time domain method (FDTD) discretizes the description of the structure and the field to values at discrete points and approximates derivatives as finite differences to solve the Maxwell's equations. The discrete dipole approximation (DDA) defines the particle by a large number of cubes, with an induced dipole for each cube, where the local field is the sum of the incident and retarded fields of the other N-1 dipoles.

In order to investigate the fundamentals of SERS, nanofabrication techniques such as electron beam lithography and focused ion beam patterning have been utilized to produce SERS-active substrates. For example, silver particle arrays [25] and gold nanohole and nanodisk arrays [26]

with precisely controlled size and spacing fabricated by electron beam lithography have been investigated. The electromagnetic coupling varies due to different diameters of the features and different distances between the features, which can determine the wavelength of the localized surface plasmon resonance (LSPR) and change the SERS effects of the arrays. In these studies, the main contribution of the enhancement is usually explained by a near-field dipole interaction within the narrow interstitial junctions between the features, and the long-range interaction in periodic arrays of particles could be also an additional source for the total enhancement [23, 24].

Besides the well-organized noble metal arrays, some relatively random metal nanostructures have been fabricated as SERS-active substrates with high reproducibility, stability and sensitivity, such as silver nanowire layers by Langmuir-Blodgett technique [30, 31], nucleation and growth of silver nanoparticles or nanorods by chemical reduction process [32, 33], and some other roughened silver substrates [60–65]. Au aggregates [66], and Au nanobowls in a random arrangement [67, 68] are also utilized for SERS. In these disordered nanostructures, such as fractal aggregates of silver or gold, an extremely high SERS enhancement is often observed on some so-called "hot spot" sites. Besides previously discussed coupling effects, Stockman and coworkers proposed a self-similar system containing different sizes of particles arranged in a chain. They argued that this structure can work as a nanolens to focus and concentrate the optical energy from bigger spheres to smaller ones, which can result in an extremely high enhancement [9, 20]. A similar mechanism was also suggested to explain "hot spots" in fractal aggregates which are disordered self-similar structures.

Chemical enhancement

The electromagnetic enhancement should be a nonselective amplifier for Raman scattering by all molecules adsorbed on a particular surface, but the molecules CO and N_2 differ by a factor of 200 in their SERS intensities under the same experimental conditions. The polarizabilities of the molecules are nearly identical and even the most radical differences in orientation upon adsorption could not produce such a large difference. In addition, Raman spectra display discrete intensity fluctuations in several Raman modes when measuring the Raman spectra of an identical molecule at different times [69]. These can be explained by chemical in-

teractions between the analyte molecules and the metal particles which yield a Raman enhancement process [70, 71]. Due to a direct chemical bond existing between the molecule and the metal, instead of Raman by isolated molecules, we need to consider a system of molecules bonded to a metal, which has different properties.

Three different situations are often grouped together as the contributors for chemical enhancement [72]. Firstly, the enhancement can be from ground state chemical interactions between a molecule and a nanoparticle that are not associated with any excitations of the nanoparticle-molecule system. It is not a resonant Raman process, but it arises during the analyte adsorption on a metal cluster. Therefore, it depends on the local environment such as the size, charge, binding site and orientation of the cluster with respect to the molecule, rather than the whole metal particle. Secondly, in a resonant Raman enhancement the excitation wavelength is resonant with a molecular transition. The frequency of incident light is chosen in a way that it crosses the frequencies of electronic excited states and resonates with them. The third situation is a charge-transfer (CT) resonant Raman enhancement. The nanoparticle-molecule system has an additional energy level due to CT and additional possible transitions between energy levels. Incident radiation induces excitation to new charge-transfer states being resonant with the nanoparticle-molecule CT transitions. This could be considered as a chemical effect analogous to the resonant Raman processes.

2.2.3 Integration and developments of sensor devices

Integration concept

The research on practical developments of SERS has mainly focused on two issues. Besides making high quality SERS-active substrates discussed in the previous section, the integration of SERS sensor chips is of particular interest to realize a remote or an easy Raman measurement.

The integration concept usually includes three parts: i) a SERS-active sensor area to absorb analyte molecules and to promote their Raman signal, ii) an optical channel to induce the excitation laser light and to collect the Raman signal, and iii) a channel to guide the molecules. Some integrated sensor chips such as a silicon-based SERS substrate fabricated by a femtosecond laser [73], a multi-mode optical fiber and a microchannel embedded in a glass substrate [74] have been demonstrated. Another al-

ternative is to use a liquid-core waveguide as the optical channel and also as the channel to guide the molecules adsorbed with silver nanoparticles [75].

Another interesting integration approach is to produce metal nanostructures on the end of optical fibers (SERS probes), which is promising for remote sensing applications [76]. The optical fiber is used for the input and collection of light. The SERS-active sites are produced on the end of fibers by the methods which have been used to make normal SERS-active substrates, such as evaporation [77], wet-etch procedure [78], focused ion beam [79], electron beam lithography [80], and femtosecond laser fabrication[81]. A tapered fiber-optic tip is designed as an optimized geometry, which can increase the area covered by the SERS coating and bring greater number of internal reflections at the interface between the fiber and the SERS coating, and thus improve the performance [82, 83].

Developments based on SERS

Low-resolution Raman spectroscopy is implemented with low-cost lasers and miniature low-resolution spectrometers to build low-cost instrumentation for the identification and analysis of organics [84–87]. Besides common Raman microscope systems, some other techniques based on SERS have also been developed. A metallized cantilever tip is controlled at the vicinity of SERS-active substrates to generate near-field enhanced Raman spectra, named as tip-enhanced Raman spectroscopy [88]. Wavelength-scanned surface-enhanced resonance Raman excitation spectroscopy involves the measurement of the SERS enhancement for several laser excitation wavelengths [89].

2.3 Metal enhanced fluorescence

Fluorescence detection is widely used in biological research. Improving fluorescence sensitivity to allow single-molecular detection is a great challenge in many applications. Lokowicz and his coworkers proposed a combination of fluorescence, plasmonics and nanofabrication to increase the capabilities of fluorescence technology, and gave it a new name - metal enhanced fluorescence [10].

A Jablonski diagram (Fig. 2.4 (a)) for fluorophores presents the fluorescence process in the free space condition from the energy level point of

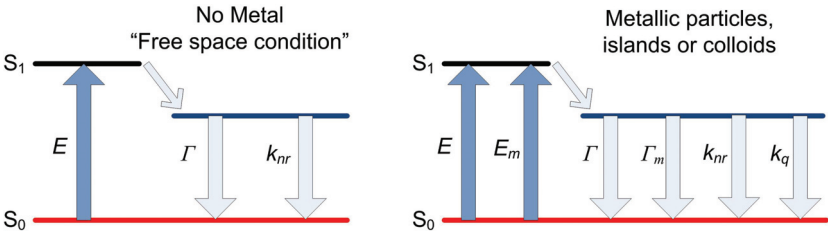

Figure 2.4: (a) Jablonski diagram for the free-space condition, (b) the modified form in the presence of metallic particles.

view. Using a beam of light (the incident electric field E), the molecules are excited from the ground electronic state (S_0) with a lower energy to a vibrational state (S_1) with a higher energy, the corresponding quantum yield (Q_0) reflects a competition between a radiative decay and non-radiative processes:

$$Q_0 = \frac{\Gamma}{\Gamma + k_{nr}},$$

where Γ and k_{nr} are the decay rate by a radiative decay process, and a non-radiative process, respectively. When the fluorophore is in the close vicinity of metal particles, the diagram of energy levels is shown in Fig. 2.4 (b). An increased intensity of local incident electric field E_m is included because of the presence of metal particles, and the corresponding quantum yield (Q_0) is modified as:

$$Q_0 = \frac{\Gamma + \Gamma_m}{\Gamma + \Gamma_m + k_{nr} + k_q},$$

with an additional radiative decay rate Γ_m as a result of the enhanced local field E_m on the fluorophore [90]. The key point in the metal enhanced fluorescence is to increase the part of radiative decay rate Γ_m by tailoring the electromagnetic environment and mastering the local environment of the fluorophore (E_m here), which can improve the quantum yield and thus increase the molecular detection efficiency. However, a quenching effect k_q is also added by damping of the dipole oscillations because of the presence of metal particles; the final quantum yield will be determined by the competition of these two additional effects [91].

2.4 Molten salt ion exchange

Glass is an interesting substrate material for integrated optics because of its relatively low cost, excellent transparency, and high threshold to opti-

cal damage. Considering the sensor applications, glass is also a relatively inert material to the bio-molecules. Ion exchange is a well-known technique proposed and developed since 1970s, to modify the electrical and optical properties of glass and to fabricate integrated optical devices such as waveguides. In the ion exchange process, some of the ions in the glass matrix (usually Na^+) are replaced by the ions of the same valence from the surrounding medium. Consequently, this replacement can change the refractive index of the host material.

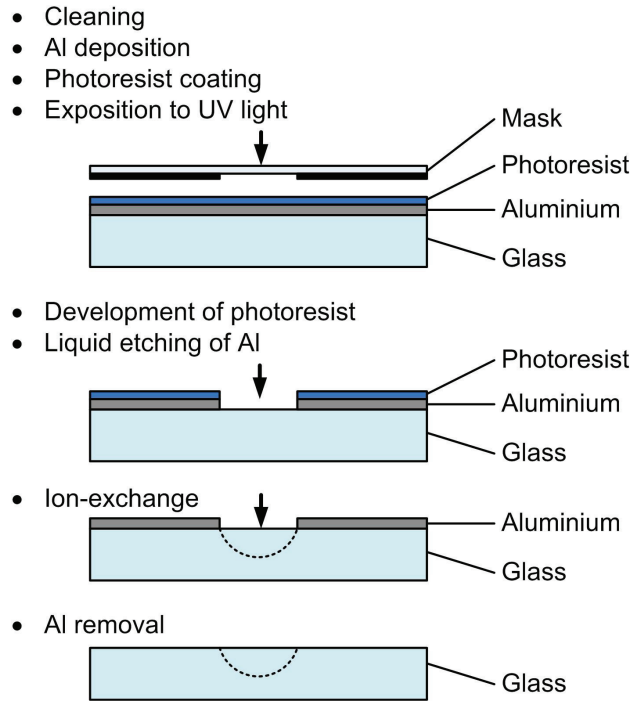

Figure 2.5: Step-by-step procedure for the channel waveguide fabrication by ion exchange.

The process to fabricate a channel optical waveguide in a planar substrate by ion exchange is shown schematically in Fig. 2.5. After cleaning, an aluminum layer is deposited on the substrate and patterned with photolithography as the mask. Dielectric masks (usually a thermally oxidized metal film) can also be used when fabricating passive waveguides. The whole substrate is immersed into molten salt containing the ions to be introduced in the glass, in a temperature controlled furnace. After removing the residual salt and the mask, a bare glass surface with an ion-exchanged channel has been formed.

A convenient approach in ion exchange is to use a crucible furnace with a vertical chamber shown in Fig. 2.6. A substrate holder is employed to control the insertion and removal of the substrate from the exchange bath while it reaches the desired temperature. For most purposes the furnace should be able to maintain and control the temperature with a range from 100 to 600 °C, through utilizing the insulated cover and thermometers. The optional stirring bar is to make the melt more homogeneous.

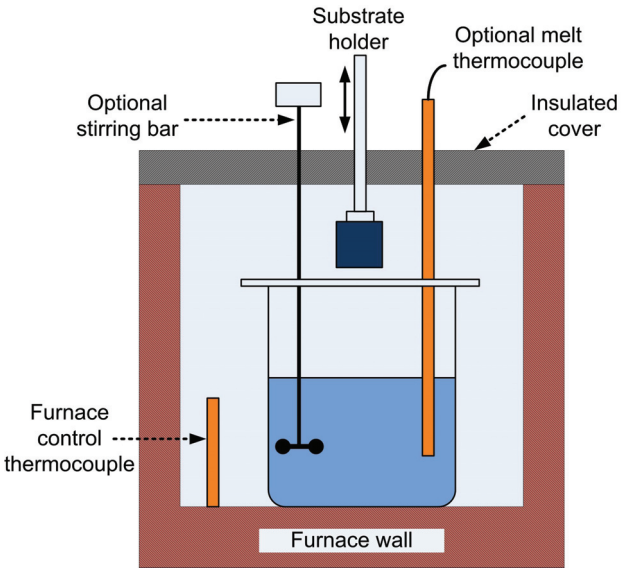

Figure 2.6: Furnace and an ion exchange apparatus cross section.

Molten salt ion exchange is a purely thermal process. There is a difference of the concentrations of the two exchanged ions between the glass and the salt melt, and the mobility of ions in glass increases at an elevated temperature. This drives a balanced diffusion replacing the original ions in the glass by the ions from the melt. The change in glass composition locally increases the refractive index of substrate glass.

There are several types of widely available glass substrates for ion exchange. The first and foremost one is the common microscope slide with high sodium content which can be easily replaced by ion exchange. For higher quality waveguides, some of the most commonly used glasses are borosilicates from Schott (BK7) and Corning (0211) because of the high sodium and potassium content and also the optical standard smoothness and flatness. There are also a variety of dopant ions to choose depending on the applications, such as Li, K, Cs, Rb, Ag, Tl, and Cu. The most common dopant for optical waveguides is Ag.

Besides the material, the temperature and duration of the ion exchange are also important factors to influence the resulting sample. The typical multi-component glasses have a softening point near 700 °C, and a annealing point in the vicinity of 550 °C. Based on the experience, the most reliable process temperatures are found at about 40 to 60 °C above the melting point of the salt, to ensure high mobility of ions in the melt while avoiding problems associated with high temperatures. At the same time, it should be less than the temperature of salt decomposition. The duration is another factor influencing the refractive index change. The longer the duration is, the deeper the diffusion can reach. For fabricating a suitable waveguide, we should combine these two factors to make a balance. In the fabrication of optical channel waveguides, Ag^+-Na^+ ion exchange with a photolithographically patterned mask is a well-established process. When a conductive mask such as Al is used, one drawback is the optical absorption and scattering losses due to the deposited metallic Ag introduced during the ion exchange process. The initial idea to generate Ag nanoparticles in glass substrates stems from this observation. This technique with intentionally enhancing the formation of Ag nanoparticles is named as a masked ion exchange (Chapter 3.4). Moreover, two other methods based on Ag^+-Na^+ ion exchange are developed, namely an ion exchange with a thermal treatment (Chapter 3.3) and a two-step ion exchange (Chapter 3.5).

3 Fabrication methods

3.1 Glass substrates

In this work, the glass substrates embedded with Ag nanoparticles include: i) commercial microscope slides (Menzel-Gläser), ii) high iron float glasses, and iii) Corning 0211 borosilicate glasses. Before the subsequent processing, all the glass substrates are cleaned by acetone and isopropanol in an ultrasonic bath, and then by a piranha solution (96% sulfuric acid (H_2SO_4) mixed with 30% hydrogen peroxide (H_2O_2) in 3:1 ratio) to remove the organic and inorganic contaminations [92].

3.1.1 Microscope slides

Table 3.1: Glass composition of microscope slides (Menzel-Gläser) [93].

Composition	Weight %
SiO_2	72.20
Na_2O	14.30
K_2O	1.20
CaO	6.40
MgO	4.30
Al_2O_3	1.20
Fe_2O_3	0.03
SO_3	0.30

The microscope slides are purchased from Menzel-Gläser with the size of $26\times76\times1.0$ mm^3. They are made of extra white soda-lime glass. The approximate glass composition of the microscope slides is presented in Table 3.1. The existence of alkaline ions enables the Ag^+ ion exchange,

and the iron ions work as a reducing agent during the formation of Ag nanoparticles by thermal annealing.

3.1.2 High iron float glasses

High iron float glasses contain high amounts of the impurity iron oxide. In the experiments, 0.016% Fe float glass and 0.361% Fe float glass, are used as the host glass to form particles. The percentage of Fe by weight in the float glasses is measured by atomic absorption spectroscopy.

3.1.3 Corning 0211

Corning 0211, available as thin wafers, is a glass with excellent optical performance. It is a high quality borosilicate glass. The glass composition of Corning 0211 is presented in Table 3.2 [94]. The size of the glass in the experiments is $50 \times 50 \times 0.5$ mm^3.

Table 3.2: Glass composition of Corning 0211.

Composition	Weight %
SiO_2	64
Na_2O	7
K_2O	7
Al_2O_3	3
TiO_2	3
B_2O_3	9
ZnO	7

3.2 Ag^+-Na^+ ion exchange

In the work, three different methods are developed to fabricate Ag nanoparticles, namely the ion exchange with thermal treatment, the masked ion exchange and the two-step ion exchange. In all of these methods, the Ag^+-Na^+ ion exchange is utilized as an essential first step to introduce Ag^+ ions into the glass matrix. The molten salt in the Ag^+-Na^+ ion exchange is the

mixture of $AgNO_3$ in a 50/50 mixture of $NaNO_3$ and KNO_3. The composition of the salt melt is chosen mainly for its convenient melt temperature, and the percentage of $AgNO_3$ can be varied from 0.1% to 5% to obtain different concentration profiles [95]. In waveguide fabrication, both the index change and the index profile are dependent on the melt composition [96]. However, in this work, Ag^+-Na^+ ion exchange is used to introduce a maximal amount of Ag^+ ions for Ag particle formation, but not to control the index change of the glass. Therefore, the highest percentage of $AgNO_3$ is chosen. The melt temperature of 300 °C is used, as previously in waveguide fabrication. The relatively long duration of 6 hours is applied for the same reason as the high percentage of $AgNO_3$.

3.3 Ion exchange with thermal treatment

Ion exchange with a subsequent thermal treatment has been used to synthesize Ag nanoparticles in soda-lime glass [35, 97–101]. Ag^+ ions are incorporated into the glass replacing the Na^+ ions of the original matrix.

In this work, the substrates are microscope slides (Menzel-Gläser). The cleaned glasses are immersed into molten salt for ion exchange as described in Chapter 3.2. The samples are then cleaned from excess salt and annealed at 500 °C for 1 h to promote nanoparticle formation. The results for these experiments are shown in publication II.

In order to understand the formation of particles, two other types of glasses containing high concentrations of iron, 0.016% Fe float glass and 0.361% Fe float glass, are also investigated. Precleaned float glasses are immersed in a molten salt mixture at 300 °C for 6 h. After the ion exchange process, the samples are post-annealed at 600 °C for 2 h. One microscope slide under the same process is used as a reference sample. The studies on high iron float glasses are presented in publication V.

3.4 Masked ion exchange

The masked ion exchange is ion exchange with a mask patterned photolithographically. The substrate used in this method is Corning 0211 glass. The masked ion exchange in silver-sodium salt melt is a well-established technique to fabricate optical waveguides [102–104]. The dif-

fuse nature of the process results in very smooth index profiles and extremely low-loss waveguides. However, metallic silver deposition at the edges of metallic masks is observed due to the existence of an Al mask [105]. The absorption and scattering losses of metallic silver could be avoided by gently etching the glass to remove the particles or by using nonmetallic masks such as aluminum oxide, silicon dioxide or silicon nitride [96], when making high-quality waveguides [106]. In this work, silver deposition in waveguide fabrication is used as an advantage, and it is used to fabricate Ag nanoparticles by intentionally enhancing the particle generation.

As shown in Fig. 3.1, a standard photolithography process is applied to make the mask pattern. The masked glass wafers are immersed in the molten salt described in Chapter 3.2 at 300 °C for 6 h. For the characterization, Al mask is removed by phosphoric acid (H_3PO_4), and different thicknesses of glass layers are etched to expose the particles using a buffered hydrofluoric acid solution (Merck Sioetch 17/02 VLSI).

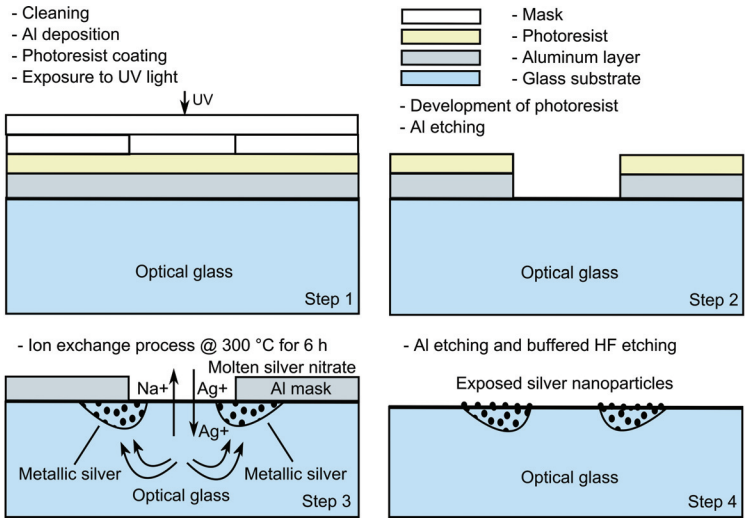

Figure 3.1: Masked ion exchange process to fabricate Ag nanoparticle pattern.

The standard photolithography process is shown schematically in Fig. 3.1 by steps 1 and 2. Firstly, a 100-nm-thick Al film is deposited on the precleaned Corning 0211 glass by an electron beam evaporator. Next, the sample is baked at 120 °C for 10 min to drive off the moisture and then primed in the adhesion promoter chemical hexamethyldisilazane (HDMS) to improve the adhesion of the photoresist to the wafer. Secondly, a pos-

itive photoresist (AZ5214) is coated by a spinner, with the speed of 7000 rpm for 20 s to produce a photoresist layer with a thickness of around 0.5 μm. A soft baking process at 90 °C for 20 min is applied to drive off the excess photoresist solvent. Thirdly, the sample is exposed under a UV light source through a prefabricated photomask for 30 s, to make the exposed photoresist soluble in the developer. After the sample is developed for 50 s in the developer (AZ351B), a hard baking at 120 °C for 10 min is done. The exposure process is done by the mask aligner (Suss MJB3 from Suss MicroTec), and the baking process is done in an oven.

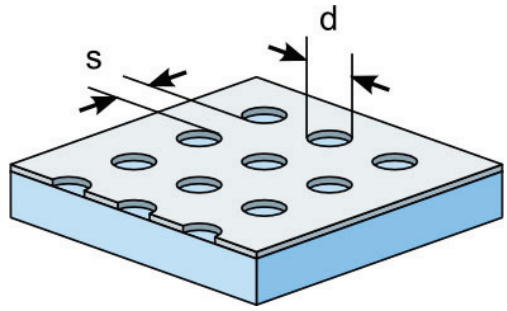

Figure 3.2: The schematic configuration of the ion exchange mask (d is the diameter of the circular holes in the pattern, and s is the edge-to-edge spacing between holes).

By optical photolithography, different patterns have been done on the Al film. As shown in Fig. 3.2, circular holes of 4 and 10 μm in diameter with the edge-to-edge spacing varying from 15 to 250 μm at different regions of the mask are studied to understand the influence of the pattern geometry in publication I, and their Raman results are reported in publication III. The stripe pattern with different opening widths and the edge-to-edge spacing of 250 μm is studied in publications II and III.

3.5 Two-step ion exchange

In the two-step ion exchange, a Ag^+-Na^+ ion exchange described in Chapter 3.2 is utilized to exchange Ag^+ ions into the Corning 0211 glass. After that, a 100-nm-thick Al film is evaporated on the ion-exchanged glass by an electron beam evaporator. The sample is dipped into a pure potassium salt (KNO_3) at 400 °C for 2 hours to promote the formation of Ag nanoparticles. In order to understand the effects of Al film and KNO_3 salt in the

formation of particles, two additional samples are fabricated: i) annealed in the air at 400 °C for 2 h with the Al layer and ii) K^+ ion-exchanged at 400 °C for 2 h without the Al layer. The processes described above for these two additional samples are also done after the Ag^+-Na^+ ion exchange at 300 °C for 6 h. The studies of these three samples are presented in publication IV.

4 Characterization methods

4.1 Optical characterization

4.1.1 UV-VIS spectrometer

The optical properties of noble metal nanoparticles are different from the optical responses of their bulk or thin film forms. The theoretical optical absorption can be calculated by solving Maxwell's equations for the scattering of electromagnetic waves of spherical objects, as carried out by Mie [52]. For the experimental results, the absorption is usually obtained by directly recording the spectrum in an ultraviolet-visible (UV-VIS) range when the particles are excited with a UV-VIS light source.

The spectrometer used to characterize surface plasmons in Ag nanoparticles is Perkin Elmer Lambda 950. The prealigned and prefocused deuterium and tungsten halogen light sources provide a wide range spectrum from 175 to 3300 nm. The UV-VIS spectral resolution reached is 0.05 nm. The double optical path configuration gives a convenient way to compare the sample and the reference directly. It is suitable when measuring the optical responses from the Ag aggregates covering a large area of the glass substrate. However, for the Ag nanoparticle patterns with the size in a μm-range, an additional microscope module is needed to image the small patterns.

4.1.2 Setup

The samples with very small features down to a micrometer and nanometer size are difficult to measure with a standard commercial spectrometer such as Perkin Elmer Lambda 950. Extraction of the influence by the small features from the large background imposes severe requirements on the instruments. Particularly, it is important to locate the position of the features. Therefore, a setup combining a microscope and a UV-

VIS spectrometer is built to measure the absorption / transmission of Ag nanoparticle patterns with the diameter of 10 μm.

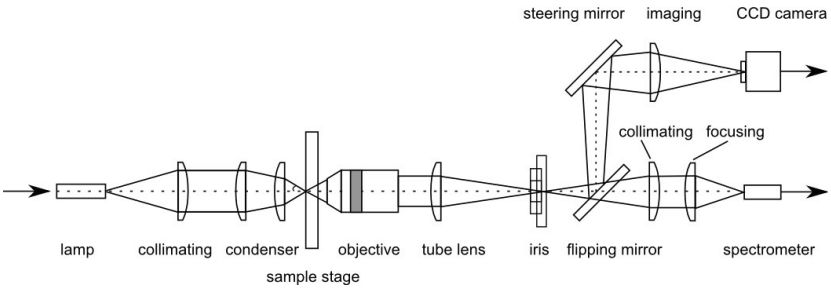

Figure 4.1: Absorption / transmission setup for Ag nanoparticle patterns.

The setup is shown in Fig. 4.1. The resonance peak of Ag nanoparticles is usually in the range of 400 to 600 nm, according to their size, shape and local dielectric environment. The light source (Ocean Optics, DH-2000) including deuterium and tungsten halogen sources, is utilized to provide the spectrum covering the UV-VIS range from 300 to 800 nm. The light source is fiber-coupled. The light from the output end of the fiber propagates through a collimator and a condenser built by high quality optical lenses, and is focused on the sample for illumination. The studied feature is magnified by a microscope objective (Olympus, LUCPLFLN, 60$\times$, NA=0.7) with a good UV transmission performance. The measured area is restricted by an adjustable aperture to reduce the beam size and to improve the contrast between the sample and the background. The transmitted light is then steered in one of two paths by a flipping mirror: one is coupled to a CCD camera for locating the feature position, and the other one is focused into a fiber-coupled high UV-sensitivity CCD spectrometer (AvaSpec-2048$\times$14-USB2) for measuring the spectra. The spectrometer is specifically designed for low optical power, fluorescence and UV applications. All the fibers and lenses used in the setup are carefully chosen to suit the wavelength range of the measurement.

4.2 Focused ion beam and transmission electron microscopy

Focused ion beam (FIB) is an advanced technique used in semiconductor and material sciences for site-specific analysis, deposition and milling. An FIB instrument combines a scanning electron microscope (SEM) to image

the sample in the chamber by the focused electron beam, and an ion beam setup to process the sample by the focused ion beam.

The FIB facility used in this work is a Helios Nanolab 600 system manufactured by the FEI company. The system is equipped with an additional micromanipulator from Kleinkiek. This is utilized in this work to prepare the thin transmission electron microscope (TEM) samples to observe the cross-section distribution of Ag nanoparticles. Since the substrate is unconductive glass, a 100 nm Cu layer is evaporated by the electron beam evaporator IM-9912 (Instrumentti Mattila Oy) on top of the glass substrate to avoid electron beam induced charging. The evaporation is done at a base pressure of 4×10^{-7} Torr and at room temperature. The deposition rate is 0.2-0.5 nm/s and the corresponding duration is 200-500 s. Then, a Pt strip ($14\times2\times1.5$ μm^3, length$\times$width$\times$height) is deposited by FIB at room temperature to locally protect the sample surface and to avoid curtain effects during the process. The material of Pt is induced by Ga ion beam with the current of 93 pA. The volume per dose of Pt from the gas injector is 0.5e^{-9} m^3/s. The deposition duration = cubic microns / (beam current (nA) $\times$ volume per dose) = 903 s. Ion beam assisted deposition could induce some Ga ion implantation, but it will not go through 100 nm of Cu protective layer and does not affect the glass substrate. And also, the deposition processes of Cu and Pt are both done at room temperature. Therefore, the deposition of Cu and Pt will not change the profile of Ag^+ ions or the formed Ag particles significantly.

In-situ site-selective FIB for TEM sample preparation has been described in detail in [107]. In a way similar to this tutorial, the TEM sample preparation process used in this work is shown step by step in Fig. 4.2 with some modifications suited to the samples used. In Fig. 4.2(a), two clean-up trenches are milled at the front and back of the Pt strip. The back trench ($16\times6\times3$ μm^3, length$\times$width$\times$depth) is bigger and deeper than the front trench ($14\times4\times2$ μm^3) for an easier cutting later. In Fig. 4.2(b), the lamella is cut free at left and bottom sides, and also cut at the right side leaving a small portion to hold the lamella to the bulk material. In Fig. 4.2(c) and (d), the manipulator probe is moved close to the lamella, some Pt is deposited to attach the lamella to the probe, and the lamella is cut free from the bulk substrate. In Fig. 4.2(e), the probe with the attached lamella is moved close to the lift-off grid. The lamella is glued on the grid by Pt deposition, cut free from the probe, and milled to a desired thickness, as shown in Fig. 4.2(f) and (g). The thickness of the lamella is

typically required to be less than 100 nm and even thinner than 50 nm in a high resolution TEM observation. Finally, the lamella is checked by the scanning transmission electron microscope (STEM) shown in 4.2(h), and is ready for the TEM observation.

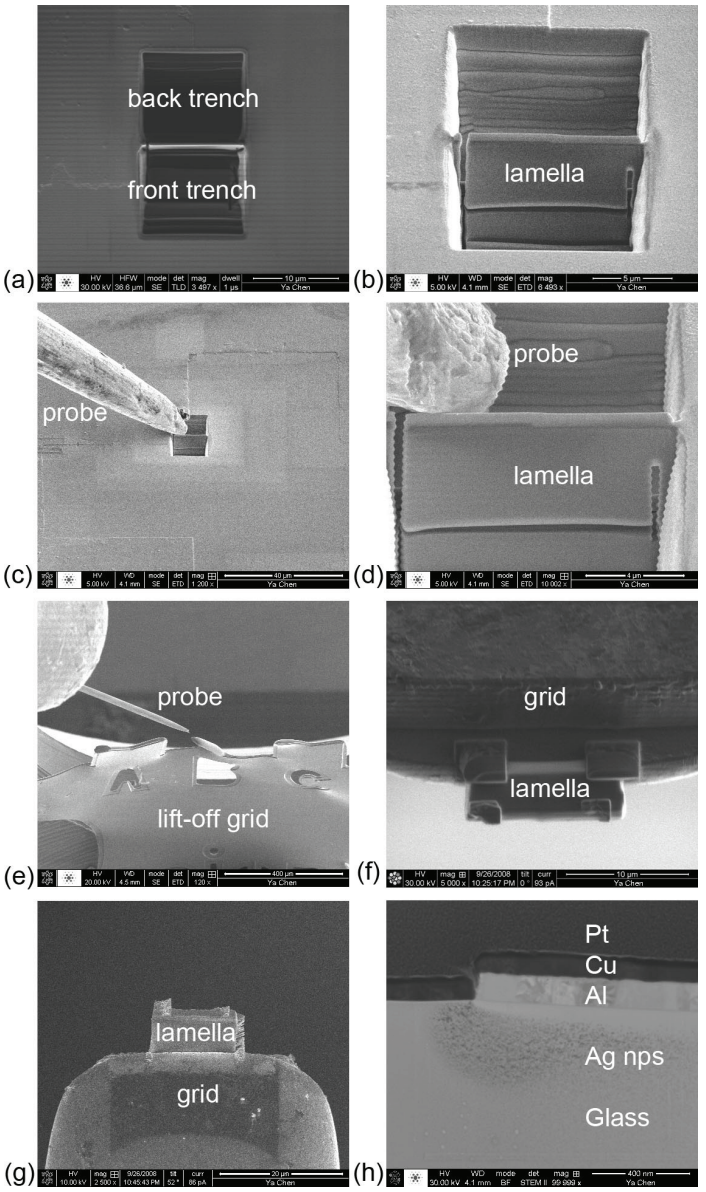

Figure 4.2: TEM sample preparation process by FIB.

Transmission electron microscopy (TEM) is a microscopy technique in which a beam of electrons is transmitted through an ultra thin specimen, interacting with the specimen as it passes through it. It is an advanced

technique not only for imaging with high resolution, but also for analyzing the material composition and observing the characteristics such as crystal orientation and electronic structure. In this work, main purposes of using TEM are to observe the cross-section distribution of particles and to confirm the material of the particles. The system FEI Tecnai F20 ST was utilized in publication I, and the system JEOL JEM-2200FS was utilized in publication IV.

4.3 Atomic force microscopy

An atomic force microscope (AFM) is one of the foremost instruments for imaging and measuring the three dimensional topography of a sample surface and also for manipulating matter at nanometer level. As shown in Fig. 4.3, AFM has a cantilever with a sharp tip at its end to scan the sample surface. When the tip is near the surface, the attractive or repulsive force between the tip and the sample results in the deflection of the cantilever. A laser is spotted on the top surface of the cantilever to measure the deflection, and reflected into a quadrant photodiode to receive the position signal. The sample is mounted on a piezoelectric stage, which can be moved accurately in all three orthogonal directions.

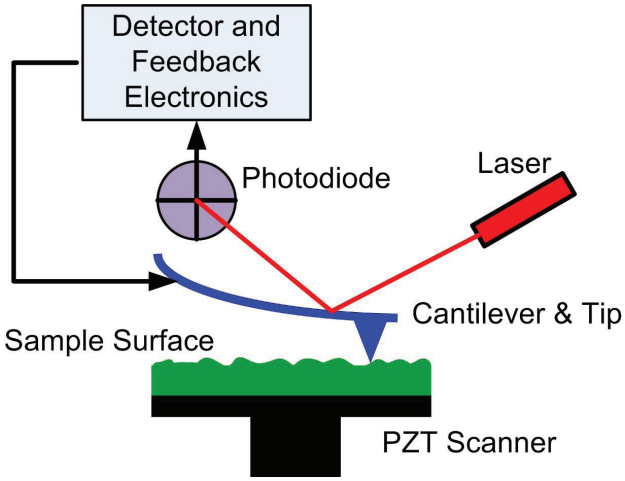

Figure 4.3: AFM principle.

To characterize the lateral distribution of particles, an AFM (NTEGRA Prima) with a semi-contact mode is employed. The maximum scanned area is 13.94×13.94 μm^2. The probe tip is a silicon cantilever highly

doped to avoid electrostatic charges. The tip typically has a curvature radius of 10 nm. Under a semi-contact mode, the cantilever is vibrated at its resonance frequency with a few nm (< 10 nm) amplitude. The force between the sample and the tip will change the oscillation frequency and amplitude. The feedback system maintains the oscillation parameters by adjusting the z position of the scanner. The topographic image is constructed by recording this position at each point.

4.4 Raman spectroscopy

As shown in Fig. 4.4, a common Raman spectrometer utilizes a laser to illuminate and to excite the sample. The scattered light from the sample is collected by an objective. The elastically Rayleigh scattered light, whose frequency is at the same position of the excited laser, is filtered out. The inelastically scattered light, including Stokes Raman scattered light and anti-Stokes Raman scattered light, is sent into the detector. It has a backscattering geometry (Fig. 4.4(a)) and a forward geometry (Fig. 4.4(b)) depending on the way of illumination.

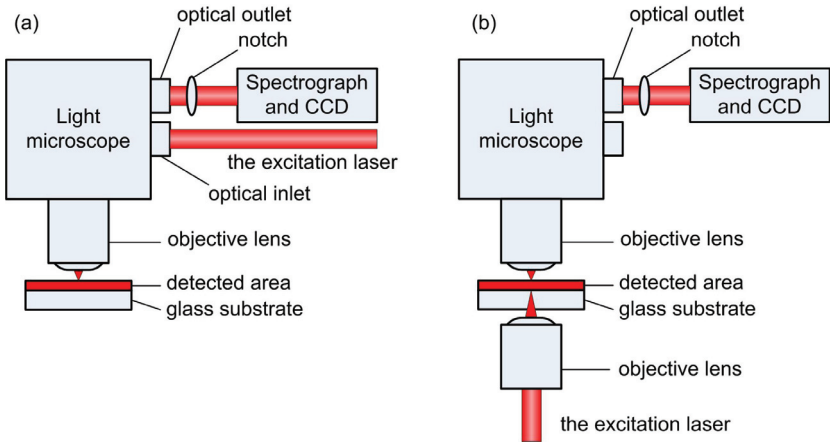

Figure 4.4: The schematic diagram of a Raman spectrometer, (a) backscattering geometry and (b) forward geometry.

The Raman system used in this work is a confocal Raman microscope alpha 300R from WITEC. The microscope uses a backscattering configuration and the excitation laser is a 532 nm frequency doubled Nd:YAG. The Raman measurements are conducted in ambient conditions.

5 Ag nanoparticle aggregates fabricated by ion exchange with thermal treatment

Ion exchange with a thermal treatment method has been introduced in Chapter 3.3. Ag nanoparticle aggregates are produced in microscope slides and high iron float glasses by this method. In this chapter, the properties and SERS activities of the formed particles are studied, and the formation mechanism is also discussed.

5.1 Depth-dependent absorption spectra of microscope slides

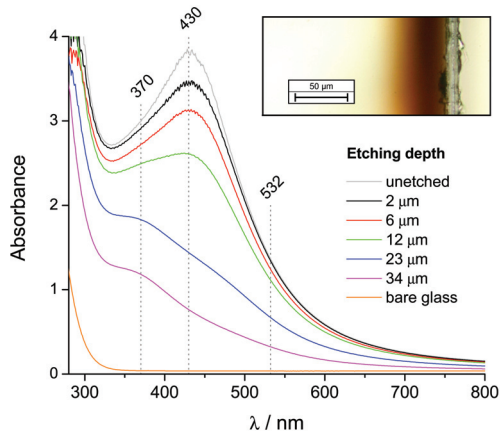

Figure 5.1: Depth-dependent absorption spectra of the ion-exchanged and annealed sample, subsequently etched at various depths.

Optical absorption spectra of the microscope slide sample, ion exchanged at 300 °C for 6 h and subsequently annealed at 500 °C for 1 h, etched at different depths are presented in Fig. 5.1. The plasmon resonance peak appears at 430 nm when the sample is unetched. With etching, the magnitude of this peak reduces rapidly, and another shoulder peak at 370 nm is seen. The absorption of the particles is influenced by various factors, mainly material, size, shape, and dielectric environment [2, 9]. In this

sample, the absorption is mainly from Ag nanoparticles inside the glass matrix. Particles at the etched surface, in addition with the very thin layer of excess Ag particles at the surface after etching, are expected to have a blue-shift in their plasmon resonance because of the decrease in effective dielectric constant of the medium, but they are so few that their contribution to the total absorption is limited. Therefore, the main reason to influence the absorption is the size of the particles. Since larger particles absorb at longer wavelenghs [108], the wide spread of the absorption covering a wavelength range of 300-800 nm suggests a continuum of particle size at any depth. The change of the peak position from 430 nm to 370 nm implies that the distribution of size varies, such that the amount of larger particles decreases with depth, but that of smaller particles increases with depth. It should be noted that the broadening of the plasmon absorption bands can be attributed not only to the particle size but also to the size distribution. The absorption peak is narrower for smaller etching depths, probably because the particles with the plasmon resonance peak close to 430 nm have a very high density in the shallow depth from the glass surface, even though the absorption is measured through a wider range of particle sizes.

In order to observe the cross-section distribution, the sample is sandwiched between two glass sheets with epoxy glue and polished into optical quality. The optical image of the cross-section of a sample is shown in the inset of Fig. 5.1. In principle, the diffusion depth of Ag^+ ions could be estimated by calculations together with a prism coupling method when there is a waveguide formed after the ion exchange [96]. However, waveguides are not typically fabricated at such a high temperature and with such a long duration, because the formed particles would cause significant losses. Moreover, in this process the diffusion of Ag^+ ions occurs during the actual ion exchange and during post-annealing. The process is developed for the generation of Ag nanoparticles but not for the fabrication of waveguides. The observed absorption by reduced Ag particles indicates the diffusion depth of Ag^+ ions. The result is given by the image, that the absorption of the particles extends some 50 μm from the surface and is gradually decreasing with depth.

In addition to the decrease of the plasmon peak, the absorption close to 300 nm is also reduced with the increase of the etching depth. It is suspected that this absorption is partially from the Rayleigh scattering of the particles, thus it can be reduced due to the decrease of the amount of Ag

particles during the etching process. In this sense, this part of loss caused by Rayleigh scattering of the particles, together with the absorption loss of the particles, can be quoted as the extinction loss of the particles. Furthermore, there are also some other possibilities besides Rayleigh scattering. For example, it could be attributed to the absorption of Fe^{3+} in the microscope slides. Fe^{3+} ions are generated with the particles in the reaction of $Fe^{2+} + Ag^{+} \rightarrow Fe^{3+} + Ag^{0}$. They have the same change in the amount as Ag particles, therefore they can cause a similar effect in the change of absorption close to 300 nm.

5.2 Absorption spectra of high iron float glasses

For understanding the effect of iron content on particle formation in float glasses, the absorption spectra of float glasses with different iron content and processed after different steps are shown in Fig. 5.2. The sample naming shown in Table 5.1 is to clarify the different processes. In the absorption spectra of the two float glasses, the absorption is mainly shown in two regions, including the overlapped peak within 300-700 nm resulting from the absorption of silver nanoparticles and the absorption of Fe^{3+} at shorter wavelengths, and the range near infrared wavelengths caused by the iron in a Fe^{2+} oxidation state [109]. The higher absorption at the infrared range in the sample #C0 than that in the sample #B0 is attributed to the higher iron concentration, which has been measured by the atomic absorption spectroscopy measurment. For both float glasses, the slight increase in absorption after ion exchange (samples #B1 and #C1) indicates that some amount of small nanoparticles have already been formed during the ion exchange. After ion exchange and post-annealing, the clear resonance peak shows around 400 nm in the spectrum of the sample #B2, and the absorption in the range of 400 to 500 nm clearly increases in the spectrum of the sample #C2. This indicates that the silver nanoparticles are mainly formed during the post-annealing process. The absorption caused by the silver nanoparticles has a broader range in the sample #C2 than in the sample #B2 due to a higher variation of nanoparticle sizes and the aggregation of nanoparticles. Furthermore, it is probably partially induced by the overlaps with the absorption of Fe^{3+} at shorter wavelengths which can be seen particularly in the spectrum of the sample #C2.

It is noted that the absorption overlap of Fe^{3+} and the Ag nanoparti-

cles is significant in the visible wavelength range, and the absorption of Fe^{2+} in the near infrared range does not change significantly after different processes, especially for the 0.361% Fe float glass. The change from Fe^{2+} state to Fe^{3+} state, caused by the formation of the silver, is inapparent. The reason is that the difference between the glass thickness and the depth of the formation of silver nanoparticles is significant. The glass thickness is about 5 mm, but the ion exchange occurs just within the depth of tens of μm for the duration of 6 h and the silver nanoparticles are formed only very close to the surface of the glass. The majority of iron ions are not changed, only a small portion of iron ions that are involved in the formation of silver nanoparticles have changed their state from Fe^{2+} to Fe^{3+}.

Table 5.1: Sample naming[1].

Material	Code	Process	Code
Microscope slide	#A	Bare glass	0
0.016% Fe float glass	#B	Ion-exchanged 300°C/6h	1
0.361% Fe float glass	#C	Ion-exchanged 300°C/6h and annealed 600°C/2h	2

[1] For example, the sample #B2 is the 0.016% Fe float glass, which is ion-exchanged at 300 °C for 6 h and post-annealed at 600 °C for 2 h.

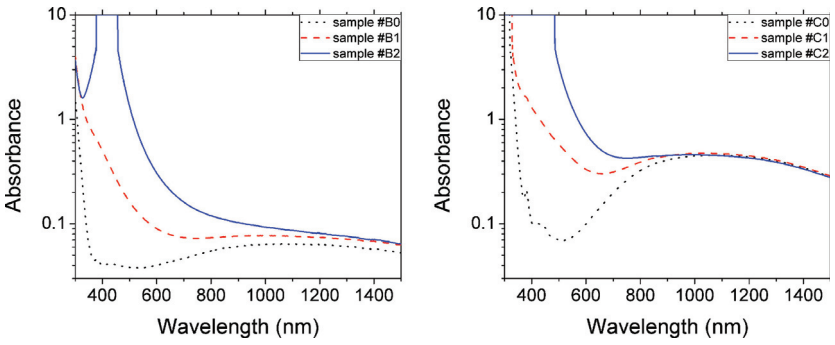

Figure 5.2: Absorption spectra measured from (a) the 0.016% Fe float glass and (b) the 0.361% Fe float glass.

5.3 Thermal reduction

When the thermal annealing is performed for the ion-exchanged glass, Ag^+ ions induced by a diffusion process are reduced to Ag atoms after capturing the electrons from the glass matrix or from the impurities.

With a sufficient source of electrons, the amount of particles generated from the glass matrix is generally determined by the concentration of Ag^+ ions. This concentration decreases with the depth from the surface due to the diffusion properties of the ion exchange process. Therefore, at a small depth, higher concentration of the Ag^+ ions results in more larger particle formation. At a larger depth, the concentration of the Ag^+ ions is low and more smaller particles are obtained. This can explain the absorption spectra of microscope slides (Fig. 5.1), where a blue shift of the absorption peak is observed when etching deeper.

In the absorption spectra of microscope slides (Fig. 5.1), some larger particles also exist at a larger depth, implied by the absorption at the longer wavelength when etching deeper. This is due to the random existence of the impurities at any depth, which are needed to reduce Ag^+ into Ag^0. Therefore, there is a chance to form larger particles or the particle aggregates at any depth. In the silver reduction process, Ag^+ ions need one electron, which they can obtain from iron when an Fe^{2+} ion transforms to an Fe^{3+} ion during the annealing process according to the reaction [97]:

$$Fe^{2+} + Ag^+ \rightarrow Fe^{3+} + Ag^0.$$

It is noted that since the ion exchange duration (6 h) is relatively long in the experiment, it can be assumed that the concentration of Ag^+ ions close to the surface after the ion exchange is almost the same as the concentration of Na^+ ions before the ion exchange. In typical sodium silicate glasses, the concentration of Na^+ is much larger than that of Fe^{2+}. In this case, the amount of particles generated from the impurities is determined not by the concentration of the Ag^+ ions but by the concentration of the Fe^{2+} ions. This can be proven by the optical spectra of high iron float glasses (Fig. 5.2).

Furthermore, the etching process could have some influence on the formation of the particles. The silver particles etched away have a possibility to aggregate with the exposed particles at the surface of the substrate and to form larger aggregates. The situation could vary between different glasses and different experiments.

5.4 Surface distribution and SERS activity of the nanoparticles

5.4.1 Microscope slides

In order to characterize the Raman activity of the samples, the microscope slides with Ag particles are etched to different depths and then incubated in Rhodamin 6G (R6G) solution for the Raman measurement. Fig. 5.3 presents a typical Raman signal of 100 nM R6G observed from the sample with different etching depths. The spectra are on the same relative scale but have been shifted in the y-direction for clarity. The inset is an optical image from a 2 μm etched sample. The Raman spectra can be only obtained from the bright spots shown in the optical image (although not from all of them). It can be seen that the typical Raman signals have about the same intensity for all the etching depths. The explanation for the background noise obtained only with the sample etched to 23 μm is unclear, and further research is needed about this point.

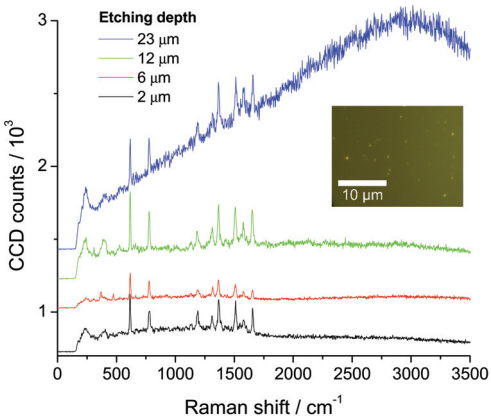

Figure 5.3: Typical Raman spectra of 100 nM R6G measured from the microscope slides etched to different depths. The inset is a representative microscope image from a 2 μm etched sample.

It can be speculated from the optical image of the cross section and the absorption spectra shown in Fig. 5.1, that formed silver particles should cover the whole substrate. The larger particles are obtained at the shallow depth, which has been discussed in the formation mechanism of thermal reduction in Chapter 5.3. However, the SERS enhancement cannot be observed everywhere on the substrate but only at some bright spots. The explanation for this could be: the density of formed particles is not

high enough to generate a strong electric field giving the high SERS enhancement. The bright spots could be the aggregates of particles which are more suitable for the SERS enhancement. They are formed around the impurities which may appear at any depth.

Because the SERS signal can only be obtained at some of the bright spots and they locate just at few places on the sample, microscope slides are not considered as a very promising host to fabricate practical SERS-active substrates. It is noteworthy that iron concentration of microscope slides is relatively high in the reported composition, but the measured absorption at near infrared wavelengths is significantly lower than that in the two float glasses. This indicates that most of the iron in microscope slides might be in the Fe^{3+} form, which does not promote the silver reduction.

5.4.2 High iron float glasses

Fig. 5.4 shows an optical image and SEM images of the samples #B2 and #C2 etched to 1.75 μm. The formed silver nanoparticles show similarly random structures all over the sample surface, with much higher density compared to the bright spots in microscope slides shown in Fig. 5.3. It can be seen that the particles have been formed into clusters that resemble the fractal clusters of silver nanoparticles shown in [9]. In sample #B2, the aggregate chains are formed by the small particles. In sample #C2, the particles appear as larger aggregates with a rough surface, which might be caused by the more efficient reduction because of the higher iron concentration.

The Raman spectra of 1 μM R6G obtained from the sample #B2 and #C2 with a 20$\times$ objective are shown in Fig. 5.5. The SERS signal can be measured over the entire sample without the need to focus on any particular position or the need to use high magnification, which is a very important feature in practical applications of SERS-active substrates. Although significantly higher surface density of silver nanoparticles are formed in the sample #C2 as suggested by the SEM images, only a moderately higher Raman signal is observed in the sample #C2 than in the sample #B2. Therefore, the aggregate chains in the sample #B2 have a better efficiency for SERS enhancement than the larger aggregates in the sample #C2. It is generally believed that locations with sharp peaks in the shape of nanoparticles and with narrow gaps between particles can result in a

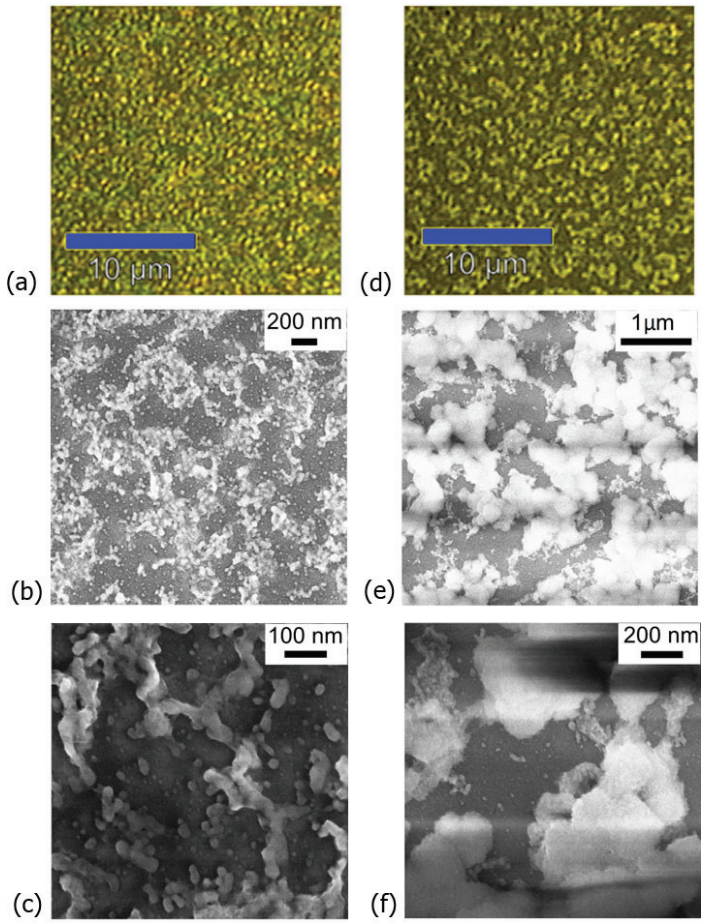

Figure 5.4: The optical images and SEM images of the sample #B2 (a, b, and c) and the sample #C2 (d, e, and f) etched to 1.75 μm.

higher electric field and better SERS enhancement. A self-similar chain of metal nanospheres has been modeled as a nanolens which can focus the plasmon field to a small gap between the nanospheres [110]. Also, the fractal aggregates of metal nanoparticles with a self-similar structure have been proposed in [9]. However, the exact characteristics of disordered metal nanoparticle structures required for optimal SERS performance are not known. Therefore, it can mainly be said that the aggregates in the sample #C2 that show the growth of nanoparticles into clusters of larger size, though containing higher surface density of silver metal, appear to have proportionally fewer SERS "hot spots".

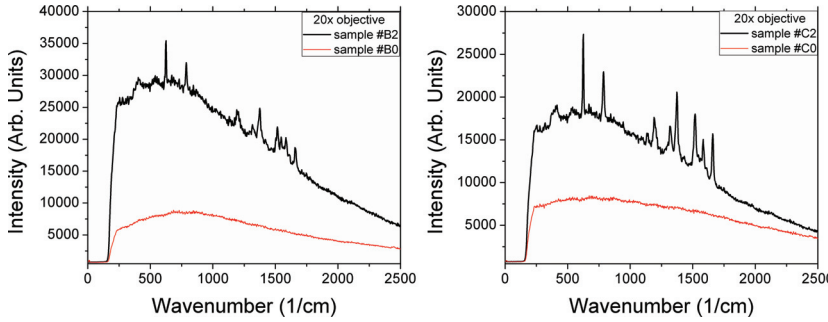

Figure 5.5: Raman spectra of 1 μM R6G measured with a 20$\times$ objective from (a) the sample #B2 etched to 1.75 μm, and (b) the sample #C2 etched to 1.75 μm.

5.4.3 Enhancement factor of SERS-active substrates

To determine the enhancement between SERS and normal Raman scattering, the enhancement factor G for SERS-active substrates has been simply defined with the expression in literature [111]:

$$G = \frac{I_{surf}}{I_{Raman}} \times \frac{N_{Raman}}{N_{surf}},$$

where N_{Raman} and N_{surf} denote the number of R6G molecules which contribute to the normal and enhanced signal respectively, while I_{Raman} and I_{surf} denote the corresponding normal Raman and SERS intensities.

However, in this definition, it is often quite difficult to observe the normal Raman intensity since it is a very weak signal which might not be visible in the spectra in some cases. Also, the exact number of molecules is difficult to determine due to the experimental limitations. Therefore, some estimations and assumptions are needed in order to calculate the enhancement factor. Based on different estimations and assumptions, different calculation methods are used. In this work, R6G is used as the analyte. Since its fluorescence signal is usually much higher than the normal Raman signal and visible in the spectra, one way is to transfer the comparison between the intensity of SERS signal and the normal Raman signal to the comparison between the intensity of SERS signal and the fluorescence signal. It is known that, under the same experimental conditions, the intensity of the normal Raman signal and that of the fluorescence signal have the following relationship [32]:

$$\frac{I_{Raman}}{I_{flu}} = \frac{\sigma_{Raman}}{\sigma_{flu}} = \frac{10^{-25}}{10^{-16}} = 10^{-9},$$

where σ_{Raman} and σ_{flu} are the cross section of the normal Raman scattering and the fluorescence when R6G is excited with the excitation at the wavelength of 514.5 nm, and they are 10^{-25} and 10^{-16} cm^2/sr respectively [17, 112]. The cross section is different when applying different excitation wavelengths. However, since in this work the excitation wavelength (532 nm) is close to that in [32], the enhancement factor can be estimated as:

$$G = \frac{I_{surf}}{I_{flu}} \times \frac{N_{Raman}}{N_{surf}} \times 10^9,$$

where I_{flu} is the fluorescence intensity under the same experimental conditions with the normal Raman scattering.

In the experiment, the fluorescence is obtained from the bare iron float glass which is considered as the unenhanced case, the SERS signal is obtained from the silver particles formed in iron float glass which is considered as the enhanced case. It is assumed that the density of molecules per surface area is the same in the enhanced and unenhanced case since both are incubated and measured in the same way. Furthermore, on the bare glass (unenhanced), the substrate is flat and the effective area of the surface is equal to that of the laser spot. On the silver particles (enhanced), for example in Fig. 5.4, the substrate has a rough surface and the effective surface area is larger than the laser spot area. If the partially embedded nanoparticles are simplified as hemispheres on a flat substrate, the factor up to 2 can be taken as the ratio of the effective area on the silver particles and on the bare glass, and the SERS enhancement factor can be written in the following form:

$$G = \frac{I_{surf}}{I_{flu}} \times \frac{A_{Raman} \div S_{R6G}}{A_{surf} \div S_{R6G}} \times 10^9 = \frac{I_{surf}}{2 \times I_{flu}} \times 10^9,$$

where S_{R6G} is the effective occupied area of a single R6G molecule under the experimental conditions, A_{Raman} and A_{surf} denote the effective area for the normal and the enhanced scattering, respectively. By substituting the intensities of the SERS signal (without the fluorescence background and noise) and the fluorescence (without the noise) at 1363 cm^{-1} as shown in Fig. 5.5, the value of the enhancement factor is estimated to be 0.3×10^9 and 0.6×10^9, respectively for the sample #B2 and #C2 in Fig. 5.5. It is comparable with the results in the literature using R6G as the analyte [30, 32, 73].

The actual enhancement factor can be different at different locations and the Raman signal from the molecules at "hot spots" can dominate in the SERS response, so this gives at best an average value and provides a comparison of the SERS responses from different substrates.

6 Ag nanoparticle patterns fabricated by masked ion exchange

6.1 Optical properties

6.1.1 The influences of the pattern geometry

The masked ion exchange method has been introduced in Chapter 3.4. The optical properties of the samples made by this method are studied here. In order to measure the absorption of small patterns with a μm size, a setup in Fig. 4.1 is built to magnify and locate the pattern. Fig. 6.1(a) shows the measured transmission spectra of masked ion-exchanged 10 μm circular patterns with different edge-to-edge spacings from 15 to 250 μm. The localized surface plasmon resonance (LSPR) wavelength and the percentage of the transmission dip change with the spacing distance, as presented in Fig. 6.1(b). The plasmon peaks red-shift from 399.48 to 438.49 nm with the increase of the spacing distance, and the transmission dips decrease with the increase of the spacing distance indicating the increase in the amount of formed Ag nanoparticles. For 10 μm openings, these changes are not so obvious when the spacing distance is more than 150 μm.

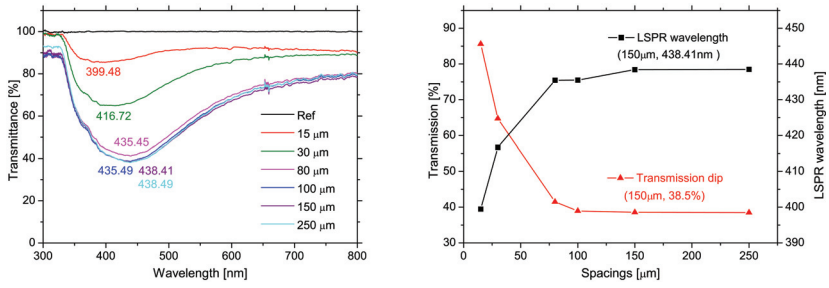

Figure 6.1: (a) Transmission spectra of silver nanoparticles for 10 μm circular patterns with different spacings. The reference spectrum is from a fully masked area of the sample. (b) The changes of transmission dip intensity and the LSPR wavelength from the same sample.

6.1.2 Formation mechanism: electrolytic deposition

Fig. 6.2 shows the electrolytic deposition of silver under the edge of the Al mask during ion exchange. The following mechanism has been used to explain this deposition [105]: During the ion exchange in a salt melt source, due to the better activity and mobility of Na^+ ions than that of Ag^+ ions, more Na^+ diffuse out of the glass than Ag^+ is diffusing in, thus an electric potential arises between the glass and the melt. In addition, the Al mask has the trend to release the electrons to Ag^+ ions in glass, and the left Al^{3+} ions intend to go into salt, resulting in another electrochemical potential between the Al mask and the melt. This electrical potential difference leads to an ionic current flowing in glass between the melt and the mask. In the regions close to the mask edge, the current and Ag^+ ions are concentrated, and the unbalanced excess silver is reduced to metallic form after capturing electrons from the Al mask.

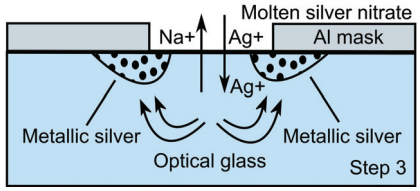

Figure 6.2: Proposed electrolytic deposition of silver under the edge of the Al mask during ion exchange.

Since the ion current is determined by the factors of electrical potential difference and the resistance of the Al mask, and the resistance depends on the mask pattern, the geometry of the mask pattern can influence the amount of metallic silver deposition. The optical results in Fig. 6.1 can be understood by this mechanism. With less densely spaced patterns the resistance of the Al film is reduced, so the ion current and thus the amount of the deposited silver are increased. When the spacing distance is above a critical value, the resistance is small enough to saturate the ion current. Not the resistance of the Al film anymore, but some other factors such as the conductivity of the glass limit the increase of the current. This can explain that the intensity of the transmission dip decreases and the dip position red-shifts with increasing the spacing distance, and this change is not obvious after the spacing achieves some critical value. In addition, the spacing distances are at the level of several microns. They were designed in the mask to study their influence to the formation of Ag particles.

6.2 Distribution of the nanoparticles

6.2.1 Cross-section distribution

A thin lamella with the thickness under 100 nm is prepared by the FIB system and observed by TEM. The preparation process has been described in detail in Chapter 4.2. Since the host glass is essentially transparent to the transmitted electron beam, the TEM image shows many layers of particles within the thickness of the lamella all superimposed together. The lamella is selectively extracted from the sample underneath the mask edge of a 10 μm circle pattern. Fig. 6.3(a) shows that the shape of the particles is nearly spherical and the average size is about 5-10 nm. Some of the small particles aggregate together and form into larger ones. The inset of this image gives the electron diffraction pattern from this area indexed as cubic silver, which proves the crystalline metallic structure of the nanoparticles. The cross-section distribution of silver particles is shown in Fig. 6.3(b). In addition, as shown in Fig. 6.3(c), X-ray energy dispersive spectroscopy (EDS) gives the element analysis from the sample. The elements other than Ag in the spectrum are from: Pt-deposit layer, Cu-deposit layer and TEM grid, Al-mask, Ga-focused ion beam, Si/O-glass.

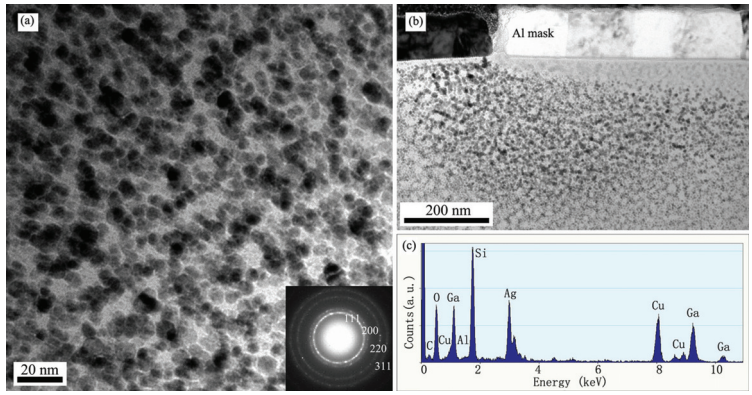

Figure 6.3: (a) Bright field image of silver nanoparticles and their electron diffraction pattern. (b) The overview image of silver nanoparticles underneath mask edge for 10 μm circle pattern. (c) EDS spectrum of element analysis of the nanoparticles.

Moreover, it is estimate from Fig. 6.3(a), that roughly 4 percent of the glass volume is filled with silver particles. This corresponds to about 80 percent of the maximum concentration of Ag^+ ions in Corning 0211 glass

established by a full Ag^+-Na^+ ion exchange. Therefore, a substantial portion of silver in the glass is reduced into metallic form in these regions.

6.2.2 Surface distribution

In order to expose the silver nanoparticles, wet etching is applied by the SiO_2 etchant (buffered HF, Merck Sioetch 17/02 VLSI). Because of the presence of the particles, the etched surface of the Ag embedded glass is not even and it is difficult to determine the average position of the surface. Therefore, it is assumed that the etching rate of the Ag embedded glass is the same as that of a bare Corning 0211 glass. The etching depth is 220 nm for the duration of 4 min, measured by a profilometer. Since Corning 0211 glass is a homogeneous material, the corresponding etching rate is calculated as 55 nm / min.

Fig. 6.4 shows the lateral distribution of silver nanoparticles from a 4 μm circular pattern with different spacings. The particles are exposed by removing a 55 nm thick glass layer from the surface. It clearly shows that the particles are following the edge of the mask. With increasing spacing, more particles are formed for the same mask opening size. This result is a qualitative proof to the conclusion obtained from the transmission spectra in Fig. 6.1, that changing the pattern geometry is an approach to control the particle formation such as the pattern or the amount of the particles.

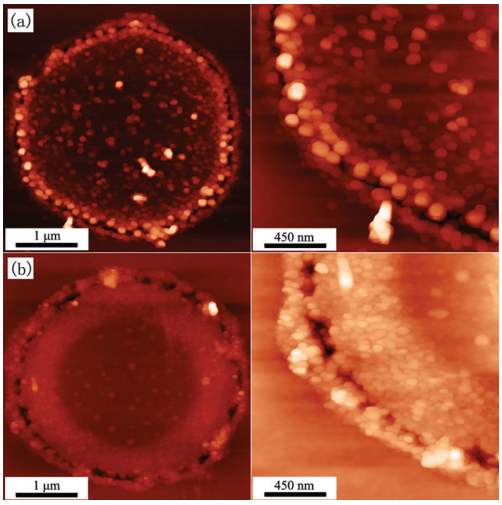

Figure 6.4: AFM micrograph of a 4 μm circular pattern with a spacing of (a) 15 μm, and (b) 100 μm.

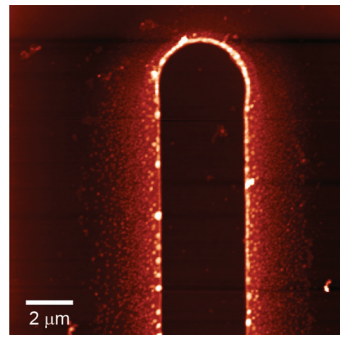

Figure 6.5: AFM image of a 4 μm stripe pattern of silver nanoparticles.

The AFM image in Fig. 6.5 presents a 4 μm stripe pattern of silver nanoparticles with the spacing of 250 μm. The optimized etching depth is 110 nm to obtain the largest density of particles. They are densely concentrated and appear as closely packed particles or aggregates along the mask edge, and getting sparser at the sites further from the mask edge. This result further confirms the patterning ability of masked ion exchange method.

6.3 SERS application

6.3.1 SERS results from the ring pattern

Since the dense aggregates of nanoparticles have been known to be the contributors to a high SERS signal [113], the ring pattern with larger spacing distance in Fig. 6.4 shows more potential for SERS due to its obvious higher density of particles. The sample is etched to the depth of 55 nm to expose the nanoparticle pattern. The Raman spectra, optical image and Raman image of 1 μM R6G obtained from this pattern are shown in Fig. 6.6. The Raman spectrum on the particles (position A) shows a clear Raman signal, while outside the particles (position B) it gives no Raman peaks but only a fluorescence background. The Raman image of the pattern presenting the intensity of the Raman signal has a similar appearance with the optical image of the pattern. It indicates that the strong SERS signal is from the locations with dense nanoparticles.

In order to study the detection limit of the substrate, the sample is incubated in different concentrations of R6G solution. The Raman spectra

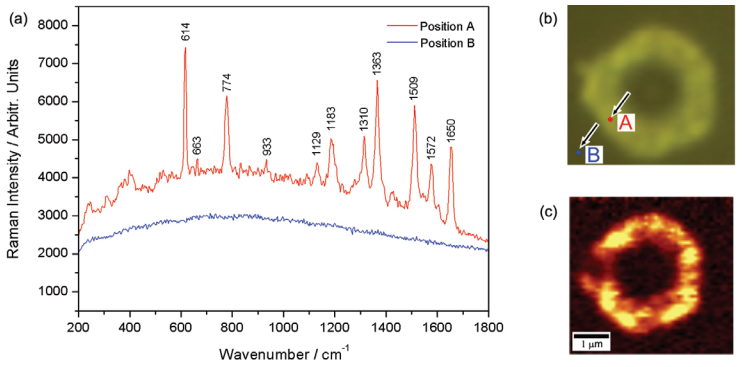

Figure 6.6: (a) Raman spectra, (b) optical image and (c) Raman image of 1 μM R6G observed from the 4 μm ring pattern of silver nanoparticles.

observed from the ring pattern for different concentrations are presented and compared in Fig. 6.7. It is reasonable that higher concentration of the solution gives better Raman signal with more resolved peaks and higher intensity of the peaks. As can be seen, R6G can be detected down to 1 nM concentration. This concentration is quite comparable with some other reported results [30, 32, 73], and some lower detection limits have been also demonstrated [61, 65]. However, the sensitivity of the SERS-active substrates is not only determined by the concentration, but also influenced by the incubation conditions (such as whether the solution is stirred or the incubation duration) and the measurement parameters (like the integration time for the spectra, the intensity of the excitation, or the magnification of the microscope objective in the Raman system). Since a relatively short incubation duration and acquisition time for a single spectrum are used, the detection limit of 1nM is a reasonably good result considering all these conditions. With the optimized experimental conditions, even better results could be achieved.

The Raman spectra are also measured for 1 μM and 10 nM R6G after storing the substrates on a shelf for one day. The SERS signal shows a decrease of roughly 50% after one day for 1 μM R6G on the ring pattern and it is much more difficult to locate the sensor spots. For 10 nM R6G, the signal disappears nearly completely after one day on the same pattern. The oxidization of Ag during the storage of the substrates in the shelf is the reason for the decrease of the SERS signal. Besides the stability of the substrate, the degradation of R6G with time could be another reason to the loss of SERS signal. This could induce a difference in the signal

decreases for different concentrations of the detected molecule. In order to improve the stability of the substrate, a thin layer of alumina can be deposited by atomic layer deposition to protect the Ag surface from oxidization. It has been demonstrated that an alumina layer with a proper thickness can provide a satisfied improvement in the stability of the SERS intensity and result in a longer lifetime of a SERS-active substrate [58].

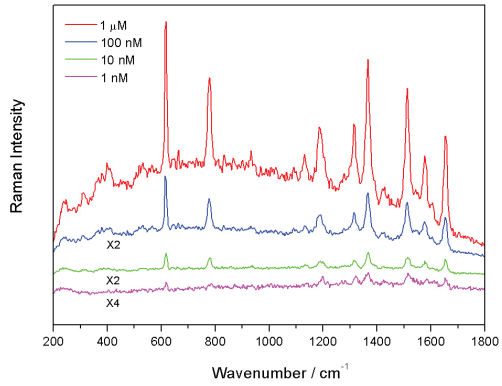

Figure 6.7: Raman spectra of R6G observed from a 4 μm ring pattern of silver nanoparticles with different concentrations in the region of 1 nM - 1 μM. The signals for the concentrations of 100, 10 and 1 nM are magnified by the factors of 2 or 4 as denoted.

6.3.2 SERS results from the stripe pattern

The distribution of particles on the stripe pattern is slightly different from that on the ring pattern. The AFM images of the stripe pattern with a 10 μm diameter, and the corresponding Raman images of 1 μM R6G observed from this pattern are shown in Fig. 6.8. The optimized etching depth for the densest particles and the best Raman signal is 55 nm for the ring pattern, but 165 nm for the stripe pattern. The explanation for this could be attributed to the formation mechanism by the masked ion exchange, presented in Chapter 6.1.2. Because of the geometry difference, a different distribution of ion current causes a different distribution of the formed particles.

However, the SERS activity of the stripe pattern is quite similar with that of the ring pattern. The dense aggregates of particles are still the better positions for the higher Raman signal, seen from the Raman image corresponding to each AFM image in Fig. 6.8. Compared to the Raman

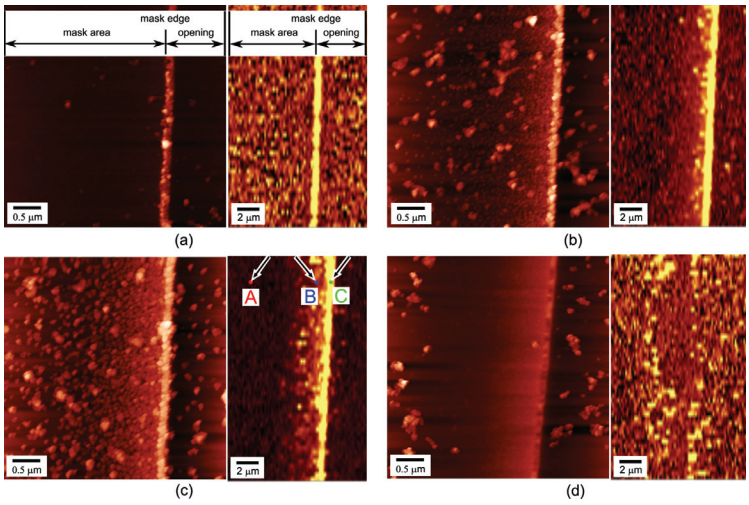

Figure 6.8: AFM images (left side) of the stripe pattern made through a 10 μm wide mask opening and Raman images (right side) of 1 μM R6G at different etching depths on the pattern. The depth increases from 55 to 220 nm from (a) to (d).

intensity of these favorable positions, it is difficult to get the Raman signal from the less dense or isolated particles and no Raman signal is obtained from the bare glass. This can be seen from the Raman spectra in Fig. 6.9, which are extracted from three different positions in Fig. 6.8(c).

Previously, the fluorescence spectrum of R6G on a thin Ag film deposited on glass has been discussed [114]. In a deposition process, never a purely smooth Ag film is formed but a rough surface with grains, which are similar with isolated Ag particles and densely packed particles depending on the deposition parameters such as thickness, deposition rate, and temperature. When a fluorophore is placed near the metal nanoparticles, two physical phenomena are involved in this process: fluorescence quenching by the metal surface and metal enhanced fluorescence. It has been noted in Chapter 2.3 that, compared to the free space conditon, an additional quenching caused by the metal surface results in the smaller quantum yield in the fluorescence, and an additional radiative decay rate as a result of the enhanced local field makes the fluorescence enhanced. In Fig. 6.9, the fluorescence spectra of three positions located in Fig. 6.8(c) are also shown. It is also noteworthy to observe and compare the fluorescence differences on these three positions. When placing the R6G molecules on the bare glass, it is the case of free space condition. When placing the

R6G molecules on the isolated particles, the quenching effect is stronger than the enhancement, and the resulting fluorescence is finally quenched. When placing the R6G molecules on the closely packed particles, the enhanced electric field is stronger than that of the isolated particles. With this strongly enhanced electric field, higher radiative decay rate can be obtained to increase the final quantum yield, thus the fluorescence is enhanced. This result shows the potential application of these produced particles for metal enhanced fluorescence.

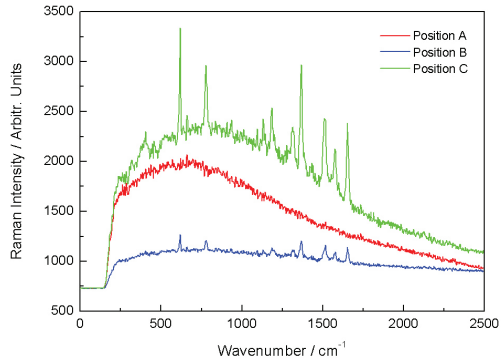

Figure 6.9: Raman and fluorescence spectra observed from position A (bare glass), B (isolated nanoparticles) and C (closely packed nanoparticles) in Fig. 6.8(c).

6.3.3 Enhancement factor of SERS-active substrates

The estimation method described in Chapter 5.4.3 is utilized to calculate the enhancement factor for silver nanoparticle patterns. In this case, the enhanced signal is from the silver nanoparticle pattern, and the unenhanced signal is from a position outside the pattern, which are shown in Fig. 6.6 as positions A and B, respectively. By substituting the intensities of the SERS signal (without the fluorescence background and noise) and the fluorescence (without the noise) at 1363 cm^{-1} as shown in Fig. 6.6, the value of the enhancement factor is estimated to be at the order of 10^9 for the silver nanoparticle ring pattern in Fig. 6.6. It is comparable with the SERS results obtained from Ag nanoparticle aggregates fabricated by the ion exchange with thermal treatment on high iron float glasses, as calculated in Chapter 5.4.3.

7 Ag nanoparticle substrates fabricated by two-step ion exchange

7.1 Optical properties

Table 7.1: The processing details of three different samples.

	Process#1	Process#2	Process#3	
	Ag^+ ion exchange	Evaporation of Al film	K^+ ion exchange	Annealed in the air
Sample#1	300°C/6h	100nm	400°C/2h	-
Sample#2	300°C/6h	100nm	-	400°C/2h
Sample#3	300°C/6h	-	400°C/2h	-

Three different samples have been fabricated by the two-step ion exchange method introduced in Chapter 3.5. Table 7.1 summarizes the processing details of these three samples. Fig. 7.1 shows their optical absorption spectra. Without the deposition of an Al film (Sample#3), there is no plasmon peak showing in the absorption, implying there is no formation of Ag nanoparticles (NPs). When there is an Al film evaporated, stronger absorption and more particles are obtained when the sample is placed in the KNO_3 salt (Sample#1) than in the air (Sample#2) at the same temperature.

7.2 Formation mechanism

After the Ag^+ ion exchange for 6h at 300 °C, if the sample is just annealed in the air for 2h at 400 °C, the annealing will change the Ag^+ concentration profile by lowering the peak of the Ag^+ concentration and driving the

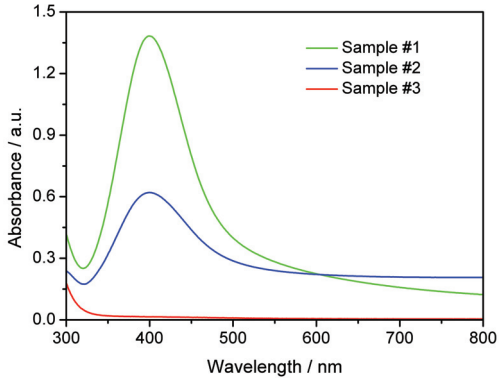

Figure 7.1: Optical absorption spectra of different glass samples with embedded Ag NPs. The samples were prepared under different experimental conditions.

whole profile deeper into the glass. However, the situation is different and more complicated in the two-step ion exchange method. The optical spectra shown in Fig. 7.1 reveal the important functions of both the Al layer and the KNO_3 salt in the subsequent process, and also give insight to the formation mechanism behind these two contributors. Fig. 7.2 gives the proposed mechanism for the formation of Ag NPs during the K^+ ion exchange with an Al layer. The Al film has an essential role during the galvanic replacement reaction, in which the Ag^+ ions are reduced into metallic Ag. The KNO_3 salt provides the possibility of an ion flow during the electrolytic deposition, in which the capability of Ag particle formation is improved by the increase of Ag^+ ions flowing from the larger depth of the glass to the vicinity of the surface of the glass.

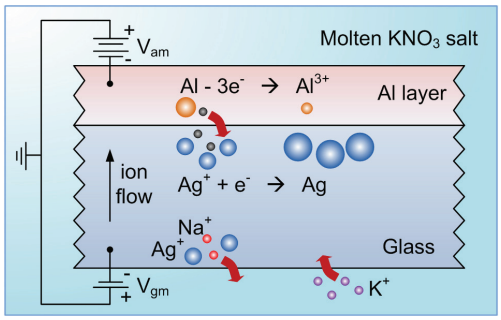

Figure 7.2: Proposed mechanism for the formation of Ag NPs during K^+ ion exchange with an Al layer.

7.2.1 Galvanic replacement reaction

The galvanic replacement provides a simple way to fabricate metal nanostructures. It usually takes place between a sacrificial metal template and a solution containing other less active metal ions. The driving force of the reaction is the electrical potential difference between these two metals, making one act as the cathode and the other one as the anode. In this work, the sacrificial metal is an Al layer and the metal ions are Ag^+ ions distributed in the glass matrix. Since the reduction potential of Al^{3+}/Al (-1.676 V versus the standard hydrogen electrode, SHE) is much lower than that of Ag^+/Ag (0.8 V versus SHE), the following redox reaction will happen:

$$Al^0 + 3Ag^+ \rightarrow Al^{3+} + 3Ag^0.$$

It is noted that, at the elevated temperature, for example 400°C at which the galvanic replacement reaction occurs in this work, the glass can be considered as a solid electrolyte, and the Ag^+ ions are relatively free to move in the glass structure, similar to the ions in a solution but with less mobility.

Since the Al layer is the critical source in the galvanic replacement reaction to provide electrons for the reduction of Ag^+ ions, the Ag particles are rarely formed without this Al layer, which is demonstrated by the absorption spectrum of Sample#3. Besides using this Al layer as the sacrificial template, an additional condition is the elevated temperature to allow the mobility of Ag^+ ions in the glass matrix. When these two conditions are satisfied, the galvanic replacement reaction can happen and Ag particles can be formed, seen from the spectra of Sample#1 and Sample#2.

7.2.2 Electrolytic deposition

Another observation is that more Ag particles are generated in Sample#1 than in Sample#2, when the sample is placed in a heated KNO_3 salt instead of heated in air. This can be referred to the electrolytic deposition which has been mentioned in Chapter 6.1.2. When the sample is dipped into the heated KNO_3 salt, the electrical potential differences between the melt, the glass substrate and the Al layer will lead to an ionic current flowing in glass and drive more Ag^+ ions from deeper in glass to the interface between the glass and the Al layer. This current can keep flowing since new ions, i.e. K^+ ions, from the melt can compensate the loss of Ag^+

ions due to the formation of Ag particles. Therefore, more Ag particles can be formed with this continuous source of Ag^+ ions. When the sample is placed in the air at an elevated temperature, the Ag particle formation can happen because of the galvanic replacement reaction, but it cannot be continued when the system attains an equilibrium because there is no continuous Ag^+ ion current flowing to the Al layer without the KNO_3 salt.

It is worthy to emphasize the difference of the electrolytic deposition in Chapter 6.1.2 and that in this section. In Chapter 6.1.2, the potential differences between the mask, the glass and the salt melt are within the distances in the micron range. In the two-step ion exchange process, the two glass surfaces in contact with the salt melt and with the mask, respectively, are separated by a 0.5 mm thick glass substrate acting as a solid electrolyte.

7.3 Distribution of the nanoparticles

7.3.1 Cross-section distribution

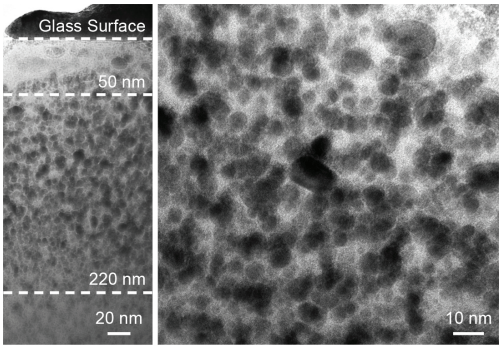

Figure 7.3: (a) The overview image showing the distribution of Ag NPs under the surface of the sample#1. (b) Bright field TEM image of the particles observed with high magnification.

For TEM studies, a TEM lamella is prepared by the FIB system introduced in Chapter 4.2. The TEM image shows the superimposed effect of many layers of particles within the thickness of the lamella, since the host glass is essentially transparent to the transmitted electron beam. The particles are nearly spherical with the diameter of 5-10 nm, seen from

Fig. 7.3(b). The size and shape of the particles are similar to the particles formed by the masked ion exchange, which are described in Chapter 6.2.1. The particles are also separated with deep and narrow gaps. However, instead of different densities of particles in a small region close to the Al mask edge, the particles formed by the two-step ion exchange are uniformly distributed under the whole Al layer and between the depths of around 50 and 220 nm from the glass surface, as shown in Fig. 7.3(a). There are also particles above 50 nm and below 220 nm, but the density of them is clearly lower than that between the depths of 50 and 220 nm.

7.3.2 Surface distribution and its Fourier analysis

The surface distribution of particles from the sample#1 etched to different depths (55, 110 and 220 nm) is shown in Fig. 7.4. The height scale shown at the bottom of each image is increasing from 220 nm to 390 nm when etching deeper. The root-mean-square (RMS) roughness of each image has been calculated as 24.2 nm, 38.6 nm, and 46.1 nm respectively, when etched to 55, 110 and 220 nm.

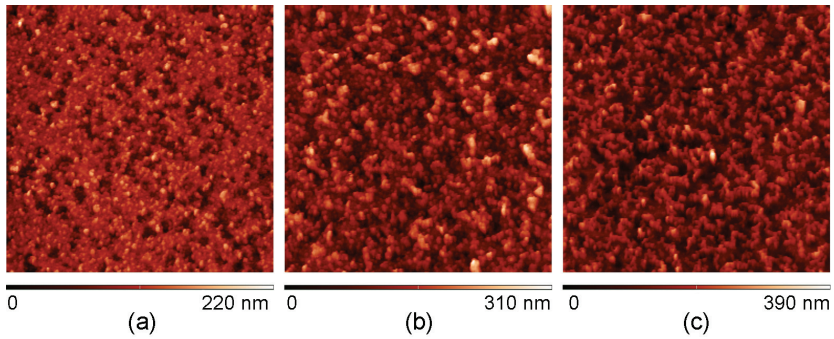

Figure 7.4: AFM images (6 μm $\times$ 6μm) scanned from the sample#1 etched to different depths (a) 55 nm, (b) 110 nm, and (c) 220 nm.

Fig. 7.5 shows two-dimensional power spectra (2D-PS) images obtained from the Fourier transform (FT) of the AFM images in Fig. 7.4. The spatial frequency domain ranges from $-(2\Delta)^{-1}$ to $+(2\Delta)^{-1}$, where Δ is the sampling interval. In this case, the sampling interval (the AFM scan step) has been calculated as the fraction of the scan length and the number of scan lines along the axes:

$$\Delta L = \Delta L_x = \Delta L_y = 23.4 \text{ nm},$$

and the spatial frequency domain ranges from [-21.33, +21.33] μm^{-1}.

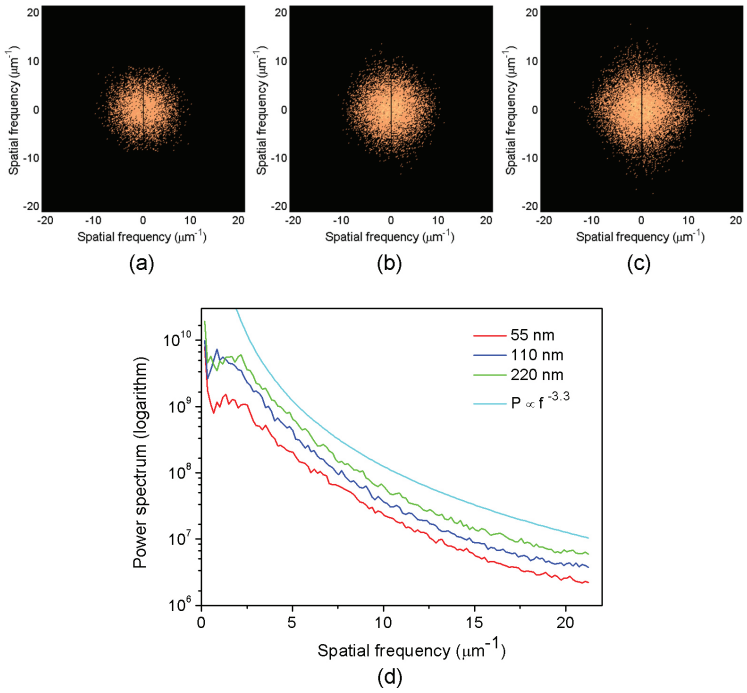

Figure 7.5: 2D-PS images of AFM images scanned from the sample#1 etched to different depths (a) 55 nm, (b) 110 nm, and (c) 220 nm; these three images have the same brightness scale. (d) the logarithmic spectra of 1D-PS integrated from the 2D-PS images, and the curve showing the function dependent on the spatial frequency to the power of -3.3.

Brightness in the 2D-PS images represents the intensity of frequency components in the surface image, and they have been rescaled with the same scale for the convenience of comparison. Using polar coordinates, the 2D-PS are integrated over the polar angle to obtain average 1D-PS. The logarithmic spectra of 1D-PS are also shown in Fig. 7.5(d). In addition, the roughness of an etched bare glass is normally less than 2 nm and sometimes less than 0.5 nm at smooth positions, which is not significant comparing to the total roughness with the particles. Therefore, the pure etching process has a negligible contribution to the roughness. However, the etching removes particles from the glass surface. These free particles have a possibility to attach to the remaining particles at the surface, which can make the surface rougher.

It is important to note that, because of the limitation of sampling in the Fourier transform, the maximum spatial frequency is 21.33 μm^{-1} and the corresponding smallest lateral size that can be resolved in AFM images

is 23.4 nm. Even with a better sampling interval, the resolution is still limited by the size of the AFM tip (usually around 10 nm). Since it has been shown in the TEM images in Fig. 7.3 that the size of the individual particles is 5-10 nm, it is impossible to resolve the individual particles in the AFM images due to the limitation related to the AFM tip. However, Fig. 7.5(d) shows that 1D-PS follow well the proportionality of $f^{-3.3}$. This power-law function is scale-invariant, which suggests that it will keep this trend when going to higher frequencies, up to the limit given by the particle sizes. Actually, this suggests a self-similar fractal structure with a fractal dimension around 1.85 [115], and the fractal aggregates of metal nanoparticles are known to be efficient for SERS [9]. Based on this surface distribution and its Fourier analysis, the evaluation of the surface features and its relation to the SERS performance will be discussed later in Chapter 7.4.2.

7.4 SERS application

7.4.1 SERS results

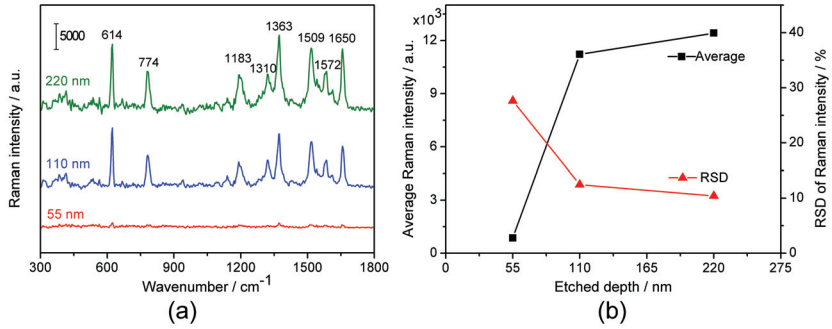

Figure 7.6: (a) Raman spectra, (b) average Raman intensity and RSD of Raman intensity of 1μM R6G observed from the sample#1 etched to different depths 55 nm, 110 nm, and 220 nm.

The Raman spectra and the corresponding data analysis observed from the sample#1 etched to different depths 55, 110, and 220 nm are shown in Fig. 7.6. The fluorescence background was subtracted in each Raman spectrum, and the average Raman intensity and the relative standard deviation (RSD) are calculated from a set of data. When etched to 55 nm, the Raman peaks are nearly invisible and the RSD is as high as 30%.

When etched to 110 and 220 nm, the Raman signals are much higher and the substrates have a good reproducibility with the RSD of 10%. With the estimation method described in Chapter 5.4.3, the highest enhancement factor is obtained on the substrates etched to 220 nm, estimated as 0.4×10^9. These results have a good agreement with the cross-section distribution of the particles in Fig. 7.3(a). The particles are not well exposed at the depth of 55 nm resulting in a low Raman signal. They are well exposed at the depths of 110 and 220 nm producing clear Raman peaks. The influence of the surface distribution is important for the SERS performance and will be discussed in detail in the next section.

7.4.2 The analysis of surface distribution and SERS results

The SERS performance depends on the amplitude of the electric field at the location where the molecule is placed. The electric field caused by the silver nanoparticles is largely determined by the arrangement of the particles, or the distribution of particles in a larger area. Therefore, the analysis of the surface distribution (the analysis of AFM images here), is helpful in understanding its influence on the SERS performance. Some methods have been utilized to quantitatively evaluate AFM images, such as standard deconvolution techniques [116], a statistical analysis of surface roughness [117], a discrete wavelet transform [118], and the Fourier transform (FT) [119]. In this work, the statistical analysis of the surface roughness and the FT are combined to study the surface features.

RMS roughness is a statistical measure presenting vertical variations in AFM images. As shown in Fig. 7.4, higher RMS roughness indicates that more rough features are obtained when etched deeper. In addition, the FT analysis of the AFM images shown in Fig. 7.5 is a way to characterize the surface features by a frequency analysis. Throughout the spatial frequency of [-21.33, +21.33] μm^{-1}, the intensity of the 1D-PS is much larger when etched to 110 nm and 220 nm than that of the sample etched to 55 nm. According to the spectra shown in Fig. 7.5(d), the intensity of the 1D-PS can be expected to keep the trend up to higher frequencies corresponding the particle sizes. The higher intensity of power spectra in frequency domain indicates larger height variation. This is in a good agreement with the height scale and the RMS roughness of the AFM images. These larger height variations indicate more roughness on the surface, which could include more "hot spots" with a better SERS signal.

8 Summary and outlook

The aim of this work was to develop fabrication methods of silver nanoparticles embedded in glasses and investigate their application for surface enhanced Raman spectroscopy (SERS). The fabrication methods based on the ion exchange technique can produce Ag nanoparticles (NPs) in a controllable way. The produced particles are proven to be suitable for biosensing applications by using rhodamine 6G (R6G) as an analyte.

Ion exchange with a thermal treatment method has been used to fabricate silver nanoparticle aggregates on microscope slides and high iron float glasses. The formation of particles in microscope slides and the SERS performance of these particles are studied in publication II. Since the SERS-active spots are only obtained at few locations, microscope slides are not considered as a very promising host to fabricate SERS-active substrates. With the increased iron concentration in high iron float glasses, much higher amount of silver particles are formed and embedded in glasses by thermal reduction. It has been demonstrated in publication V that high iron float glasses can be used as substrates to make SERS-active substrates with good performance and high reproducibility.

The formation of silver nanoparticles in waveguide fabrication by a masked ion exchange has been observed as a problem because it can increase attenuation in the waveguides. Here, the silver deposition is taken as an advantage, and it is used to fabricate Ag nanoparticles by intentionally enhancing the particle generation. The properties of these particles are studied and the formation mechanism of electrolytic deposition is discussed. Since the silver particles are only deposited at the edge of the mask, this method provides a way to make silver nanoparticle patterns. The ring and stripe patterns have been demonstrated in publications I and II, and their SERS activities have been studied in publication III. The masked ion exchange process provides a possibility to make SERS-active substrates using high quality Corning 0211 glass as a substrate. In addition, as the presented technique is also widely used in the fab-

rication of glass waveguides, it could be possible to make lab-on-a-chip devices, which integrates the silver particles with optical waveguides and microfluidic channels, for high-sensitivity surface enhanced spectroscopy.

A two-step ion exchange method has been developed to fabricate uniform nanoparticle clusters (over large areas) embedded in Corning 0211 glass in publication IV. Ag^+ ions are introduced into glass in an Ag^+ ion exchange, and reduced into metallic silver in a subsequent K^+ ion exchange. The formation mechanism is explained by a combination effect of the galvanic replacement reaction and the electrolytic deposition. The properties of the particles are characterized. Particularly the relationship between the surface distribution of the particles and the Raman spectra is discussed. Compared to the silver particles formed by the masked ion exchange, the particles formed by the two-step ion exchange are over broad areas under the Al film, and the SERS signal can be measured over the entire sample without the need to focus on any particular position or the need to use high magnification. This is a very important feature in practical applications of SERS-active substrates. Moreover, the presented method could also enable the patterning of areas with the particles when applying a photolithographic mask in either the first step of Ag^+ ion exchange or the second step of K^+ ion exchange process. Therefore, the two-step ion exchange is not only a good way to fabricate SERS-active substrates, but also an ideal option for the development of integrated sensor chips. When applying this technique on an optical fiber, a SERS probe with silver nanoparticles on the tip of the fiber could also be fabricated to realize remote detection.

These three methods used to fabricate SERS-active substrates in this thesis are all based on ion exchange processes. They are simple and low-cost methods suitable for large scale fabrication, having important significance in the commercialization of this innovation. Taking the reproducibility of the Raman signal into account, the optimal enhancement factor is on the order of 10^9, and the same level is obtained for all the substrates fabricated by the three methods in this work. Comparing their Raman signals to the other reported SERS-active substrates using R6G as the tested molecule, the optimal enhancement factor is higher or comparable with most of them [25, 30, 32, 33, 73]. Regarding the detection limit of R6G, the lowest detected concentration of 10^{-9} M has been demonstrated in this work. Similar [25, 30, 32, 33, 73] or lower concentrations [61, 65] down to a single-molecule detection [17, 73] have been detected

before. The studies and increased understanding about the fabrication of Ag NPs and the demonstration of their SERS activities provide the necessary foundations, and the logical next step is to develop integrated sensor chips based on the techniques in this thesis and to apply them in real biosensor applications. Some ideas to extend this work are: i) to fabricate integrated sensor chips for high-performance easy-to-use SERS detection; ii) to realize remote detection by fabricating a SERS-active sensor area on the tip of an optical fiber to serve as a SERS probe; and iii) to investigate the performance of the sensors in real medical or biological applications.

Bibliography

[1] G. Mie, "Beiträge zur Optik trüber Medien, speziell kolloidaler Metallösungen (Contributions to the optics of turbid media, particularly of colloidal metal solutions)," *Annalen der Physik*, vol. 25, no. 3, pp. 377–445, 1908.

[2] K. Lance Kelly, E. Coronado, L. L. Zhao, and G. C. Schatz, "The optical properties of metal nanoparticles: the influence of size, shape, and dielectric environment," *The Journal of Physical Chemistry B*, vol. 107, pp. 668–677, 2003.

[3] E. Hutter and J. H. Fendler, "Exploitation of localized surface plasmon resonance," *Advanced Materials*, vol. 16, no. 19, pp. 1685–1706, 2004.

[4] A. J. Haes and R. P. Van Duyne, "A unified view of propagating and localized surface plasmon resonance biosensors." *Analytical and bioanalytical chemistry*, vol. 379, no. 7-8, pp. 920–930, 2004.

[5] S. A. Maier, P. G. Kik, H. A. Atwater, S. Meltzer, E. Harel, B. E. Koel, and A. A. G. Requicha, "Local detection of electromagnetic energy transport below the diffraction limit in metal nanoparticle plasmon waveguides," *Nature Materials*, vol. 2, no. 4, pp. 229–232, 2003.

[6] E. Ozbay, "Plasmonics: merging photonics and electronics at nanoscale dimensions." *Science*, vol. 311, no. 5758, pp. 189–193, 2006.

[7] S. Lal, S. Link, and N. J. Halas, "Nano-optics from sensing to waveguiding," *Nature Photonics*, vol. 1, pp. 641–648, 2007.

[8] R. Kashyap and G. Nemova, "Surface plasmon resonance-based fiber and planar waveguide sensors," *Journal of Sensors*, vol. 2009, pp. 1–9, 2009.

[9] M. I. Stockman, "Nanoplasmonics : The physics behind the applications," *Physics Today*, vol. 64, no. 2, pp. 39–44, 2011.

[10] J. R. Lakowicz, "Plasmonics in Biology and Plasmon-Controlled Fluorescence." *Plasmonics*, vol. 1, no. 1, pp. 5–33, 2006.

[11] M. Moskovits, "Surface-enhanced Raman spectroscopy: a brief retrospective," *Journal of Raman Spectroscopy*, vol. 36, no. 6-7, pp. 485–496, 2005.

[12] Z. Q. Tian, "Surface-enhanced Raman spectroscopy: advancements and applications," *Journal of Raman Spectroscopy*, vol. 36, no. 6-7, pp. 466–470, 2005.

[13] J. A. Dieringer, A. D. McFarland, N. C. Shah, D. A. Stuart, A. V. Whitney, C. R. Yonzon, M. A. Young, X. Y. Zhang, and R. P. Van Duyne, "Surface enhanced Raman spectroscopy: new materials, concepts, characterization tools, and applications," *Faraday Discussions*, vol. 132, pp. 9–26, 2006.

[14] M. K. Hossain and Y. Ozaki, "Surface-enhanced Raman scattering: facts and inline trends," *Current Science*, vol. 97, no. 2, pp. 192–201, 2009.

[15] G. McNay, D. Eustace, W. E. Smith, K. Faulds, and D. Graham, "Surface-enhanced Raman scattering (SERS) and surface-enhanced resonance Raman scattering (SERRS): a review of applications." *Applied spectroscopy*, vol. 65, no. 8, pp. 825–37, 2011.

[16] M. Fleischmann, P. J. Hendra, and A. J. McQuillan, "Raman spectra of pyridine adsorbed at a silver electrode," *Chemical Physics Letters*, vol. 26, no. 2, pp. 163–166, 1974.

[17] S. M. Nie and S. R. Emery, "Probing single molecules and single nanoparticles by surface-enhanced Raman scattering," *Science*, vol. 275, no. 5303, pp. 1102–1106, 1997.

[18] K. Kneipp, Y. Wang, H. Kneipp, L. T. Perelman, I. Itzkan, R. Dasari, and M. S. Feld, "Single molecule detection using surface-enhanced Raman scattering (SERS)," *Physical Review Letters*, vol. 78, no. 9, pp. 1667–1670, 1997.

[19] A. Campion and P. Kambhampati, "Surface-enhanced Raman scattering," *Chemical Society Reviews*, vol. 27, no. 4, pp. 241–250, 1998.

[20] K. Kneipp, "Surface-enhanced Raman scattering," *Physics Today*, vol. 60, no. 11, pp. 40–47, 2007.

[21] M. Moskovits, "Surface-enhanced spectroscopy," *Reviews of Modern Physics*, vol. 57, no. 3, pp. 783–826, 1985.

[22] A. Otto, I. Mrozek, H. Grabhorn, and W. Akemann, "Surface-enhanced Raman scattering," *Journal of Physics-Condensed Matter*, vol. 4, no. 5, pp. 1143–1212, 1992.

[23] S. Zou and G. C. Schatz, "Silver nanoparticle array structures that produce giant enhancements in electromagnetic fields," *Chemical Physics Letters*, vol. 403, no. 1-3, pp. 62–67, 2005.

[24] G. Laurent, N. Felidj, J. Grand, J. Aubard, G. Levi, A. Hohenau, F. R. Aussenegg, and J. R. Krenn, "Raman scattering images and spectra of gold ring arrays," *Physical Review B*, vol. 73, no. 24, p. 245417, 2006.

[25] L. Gunnarsson, E. J. Bjerneld, H. Xu, S. Petronis, B. Kasemo, and M. Kall, "Interparticle coupling effects in nanofabricated substrates for surface-enhanced Raman scattering," *Applied Physics Letters*, vol. 78, no. 6, pp. 802–804, 2001.

[26] Q. M. Yu, P. Guan, D. Qin, G. Golden, and P. M. Wallace, "Inverted size-dependence of surface-enhanced Raman scattering on gold nanohole and nanodisk arrays," *Nano Letters*, vol. 8, no. 7, pp. 1923–1928, 2008.

[27] R. Z. Tan, A. Agarwal, N. Balasubramanian, D. L. Kwong, Y. Jiang, E. Widjaja, and A. Garland, "3D arrays of SERS substrate for ultrasensitive molecular detection," *Sensors and Actuators A*, vol. 139, pp. 36–41, 2007.

[28] C. Liusman, H. Li, G. Lu, J. Wu, F. Boey, S. Li, and H. Zhang, "Surface-enhanced Raman scattering of Ag-Au nanodisk heterodimers," *The Journal of Physical Chemistry C*, vol. 116, pp. 10 390–10 395, 2012.

[29] Q. Min, M. J. L. Santos, E. M. Girotto, A. G. Brolo, and R. Gordon, "Localized Raman enhancement from a double-hole nanostructure in a metal film," *The Journal of Physical Chemistry C*, vol. 112, no. 39, pp. 15 098–15 101, 2008.

[30] A. Tao, F. Kim, C. Hess, J. Goldberger, R. R. He, Y. G. Sun, Y. N. Xia, and P. D. Yang, "Langmuir-Blodgett silver nanowire monolayers for molecular sensing using surface-enhanced Raman spectroscopy," *Nano Letters*, vol. 3, no. 9, pp. 1229–1233, 2003.

[31] R. F. Aroca, P. J. G. Goulet, D. S. dos Santos, R. A. Alvarez-Puebla, and O. N. Oliveira, "Silver nanowire layer-by-layer films as substrates for surface-enhanced Raman scattering," *Analytical Chemistry*, vol. 77, no. 2, pp. 378–382, 2005.

[32] J. Zhou, S. P. Xu, W. Q. Xu, B. Zhao, and Y. Ozaki, "In situ nucleation and growth of silver nanoparticles in membrane materials: a controllable roughened SERS substrate with high reproducibility," *Journal of Raman Spectroscopy*, vol. 40, no. 1, pp. 31–37, 2009.

[33] S. J. Guo, S. J. Dong, and E. K. Wang, "Rectangular silver nanorods: controlled preparation, liquid-liquid interface assembly, and application in surface-enhanced Raman scattering," *Crystal Growth & Design*, vol. 9, no. 1, pp. 372–377, 2009.

[34] X. Wang and X. Liu, "Self-assembled synthesis of Ag nanodendrites and their applications to SERS," *Journal of Molecular Structure*, vol. 997, no. 1-3, pp. 64–69, 2011.

[35] J. Zhang, W. Dong, J. W. Sheng, J. W. Zheng, J. Li, L. Qiao, and L. Q. Jiang, "Silver nanoclusters formation in ion-exchanged glasses by thermal annealing, UV-laser and X-ray irradiation," *Journal of Crystal Growth*, vol. 310, no. 1, pp. 234–239, 2008.

[36] X. Wang, C. Wang, L. Cheng, S. T. Lee, and Z. Liu, "Noble metal coated single-walled carbon nanotubes for applications in surface enhanced Raman scattering imaging and photothermal therapy." *Journal of the American Chemical Society*, vol. 134, no. 17, pp. 7414–7422, 2012.

[37] P. Pinkhasova, L. Yang, Y. Zhang, S. Sukhishvili, and H. Du, "Differential SERS activity of gold and silver nanostructures enabled by adsorbed poly(vinylpyrrolidone)." *Langmuir*, vol. 28, no. 5, pp. 2529–2535, 2012.

[38] Z. Yi, X. Tan, G. Niu, X. Xu, X. Li, X. Ye, J. Luo, B. Luo, W. Wu, Y. Tang, and Y. Yi, "Facile preparation of dendritic Ag–Pd bimetallic nanostructures on the surface of Cu foil for application as a SERS-substrate," *Applied Surface Science*, vol. 258, no. 14, pp. 5429–5437, 2012.

[39] S. Y. Baik, Y. J. Cho, Y. R. Lim, H. S. Im, D. M. Jang, and Y. Myung, "Raman scattering using silver and gold nanoparticles deposited on silicon-carbon core-shell nanowires," *ACS Nano*, vol. 6, no. 3, pp. 2459–2470, 2012.

[40] I. Freestone, N. Meeks, M. Sax, and C. Higgitt, "The Lycurgus cup – A Roman nanotechnology," *Gold Bulletin*, vol. 40, no. 4, pp. 270–277, 2007.

[41] M. Faraday, "Experimental relations of gold (and other metals) to light," *Philosophical Transactions the Royal Society in London*, vol. 147, pp. 145–181, 1857.

[42] U. Kreibig and M. Vollmer, *Optical properties of metal clusters*. Springer, 1995.

[43] S. A. Maier, *Plasmonics: fundamentals and applications*. Springer, 2007.

[44] P. W. Barber and S. C. Hill, *Light scattering by particles: computational methods*. World Scientific, Singapore, 1990.

[45] W. H. Yang, G. C. Schatz, and R. P. Van Duyne, "Discrete dipole approximation for calculating extinction and Raman intensities for small particles with arbitrary shapes," *Journal of Chemical Physics*, vol. 103, no. 3, pp. 869–875, 1995.

[46] K. Shlager and J. Schneider, "A selective survey of the finite-difference time-domain literature," *IEEE Antennas and Propagation Magazine*, vol. 37, no. 4, pp. 39–57, 1995.

[47] A. Gopinath, S. V. Boriskina, B. M. Reinhard, and L. Dal Negro, "Deterministic aperiodic arrays of metal nanoparticles for surface-enhanced Raman scattering (SERS)," *Optics Express*, vol. 17, no. 5, pp. 3741–3753, 2009.

[48] S. A. Maier, P. G. Kik, and H. A. Atwater, "Observation of coupled plasmon-polariton modes in Au nanoparticle chain waveguides of different lengths: Estimation of waveguide loss," *Applied Physics Letters*, vol. 81, no. 9, pp. 1714–1716, 2002.

[49] B. Lamprecht, G. Schider, R. Lechner, H. Ditlbacher, J. Krenn, A. Leitner, and F. Aussenegg, "Metal nanoparticle gratings: influence of dipolar particle interaction on the plasmon resonance," *Physical Review Letters*, vol. 84, no. 20, pp. 4721–4724, 2000.

[50] M. Piliarik and J. Homola, "Surface plasmon resonance (SPR) sensors: approaching their limits?" *Optics Express*, vol. 17, no. 19, pp. 16 505–16 517, 2009.

[51] D. A. Stuart, A. J. Haes, C. R. Yonzon, E. M. Hicks, and R. P. Van Duyne, "Biological applications of localised surface plasmonic phenomenae," *IEE Proc.-Nanobiotechnol.*, vol. 152, no. 1, pp. 13–32, 2005.

[52] S. A. Maier and H. A. Atwater, "Plasmonics: Localization and guiding of electromagnetic energy in metal/dielectric structures," *Journal of Applied Physics*, vol. 98, no. 1, p. 011101, 2005.

[53] A. Y. Sonay, A. B. Çağlayan, and M. Çulha, "Synthesis of peptide mediated Au core–Ag shell nanoparticles as surface-enhanced Raman scattering labels," *Plasmonics*, vol. 7, no. 1, pp. 77–86, 2011.

[54] T. Y. Liu, K. T. Tsai, H. H. Wang, Y. Chen, Y. H. Chen, Y. C. Chao, H. H. Chang, C. H. Lin, J. K. Wang, and Y. L. Wang, "Functionalized arrays of Raman-enhancing nanoparticles for capture and culture-free analysis of bacteria in human blood," *Nature Communications*, vol. 2, p. 538, 2011.

[55] D. L. Jeanmaire and R. P. Van Duyne, "Heterocyclic, aromatic and aliphatic amines adsorbed on the anodized silver electrode," *Journal of Electroanalytical Chemistry*, vol. 84, pp. 1–20, 1977.

[56] M. G. Albrecht and J. A. Creighton, "Anomalously intense Raman spectra of pyridine at a silver electrode," *Journal of the American Chemical Society*, vol. 99, no. 15, pp. 5215–5217, 1977.

[57] X. Y. Zhang, J. Zhao, A. V. Whitney, J. W. Elam, and R. P. Van Duyne, "Ultrastable substrates for surface-enhanced Raman spectroscopy: Al_2O_3 overlayers fabricated by atomic layer deposition yield improved anthrax biomarker detection," *Journal of the American Chemical Society*, vol. 128, no. 31, pp. 10 304–10 309, 2006.

[58] J. F. John, S. Mahurin, S. Dai, and M. J. Sepaniak, "Use of atomic layer deposition to improve the stability of silver substrates for in situ, high temperature SERS measurements," *Journal of Raman Spectroscopy*, vol. 41, no. 1, pp. 4–11, 2010.

[59] J. R. Anema, A. G. Brolo, P. Marthandam, and R. Gordon, "Enhanced Raman scattering from nanoholes in a copper film," *The Journal of Physical Chemistry C*, vol. 112, no. 44, pp. 17 051–17 055, 2008.

[60] M. Green and F. M. Liu, "SERS substrates fabricated by island lithography: the silver/pyridine system," *The Journal of Physical Chemistry B*, vol. 107, no. 47, pp. 13 015–13 021, 2003.

[61] Y. C. Liu, C. C. Yu, and S. F. Sheu, "Low concentration rhodamine 6G observed by surface-enhanced Raman scattering on optimally electrochemically roughened silver substrates," *Journal of Materials Chemistry*, vol. 16, no. 35, pp. 3546–3551, 2006.

[62] K. Yliniemi, M. Vahvaselkä, Y. V. Ingelgem, K. Baert, B. P. Wilson, H. Terryn, and K. Kontturi, "The formation and characterisation of ultrathin films containing Ag nanoparticles," *Journal of Materials Chemistry*, vol. 18, no. 2, pp. 199–206, 2008.

[63] A. Marimuthu, P. Christopher, and S. Linic, "Design of plasmonic platforms for selective molecular sensing based on surface-enhanced Raman spectroscopy," *The Journal of Physical Chemistry C*, vol. 116, pp. 9824–9829, 2012.

[64] B. Liu, W. Zhang, H. Lv, D. Zhang, and X. Gong, "Novel Ag decorated biomorphic SnO_2 inspired by natural 3D nanostructures as SERS substrates," *Materials Letters*, vol. 74, pp. 43–45, 2012.

[65] G. Upender, R. Satjavathi, B. Raju, D. Shadak Alee, D. Narayana Rao, and C. Bansal, "Silver nanocluster films as novel SERS substrates for ultrasensitive detection," *Chemical Physics Letters*, vol. 511, pp. 309–314, 2011.

[66] C. Y. Song, Z. Y. Wang, R. H. Zhang, J. Yang, X. B. Tan, and Y. P. Cui, "Highly sensitive immunoassay based on Raman reporter-labeled immuno-Au aggregates and SERS-active immune substrate," *Biosensors & Bioelectronics*, vol. 25, no. 4, pp. 826–831, 2009.

[67] J. Ye, P. Van Dorpe, W. Van Roy, G. Borghs, and G. Maes, "Fabrication, Characterization, and Optical Properties of Gold Nanobowl Submonolayer Structures," *Langmuir*, vol. 25, no. 3, pp. 1822–1827, 2009.

[68] J. Ye, P. Van Dorpe, W. Van Roy, K. Lodewijks, I. De Vlaminck, G. Maes, and G. Borghs, "Fabrication and Optical Properties of Gold Semishells," *The Journal of Physical Chemistry C*, vol. 113, no. 8, pp. 3110–3115, 2009.

[69] D. P. Fromm, A. Sundaramurthy, A. Kinkhabwala, P. J. Schuck, G. S. Kino, and W. E. Moerner, "Exploring the chemical enhancement for surface-enhanced Raman scattering with Au bowtie nanoantennas." *The Journal of Chemical Physics*, vol. 124, no. 6, p. 61101, 2006.

[70] J. R. Lombardi, R. L. Birke, T. Lu, and J. Xu, "Charge-transfer theory of surface enhanced Raman spectroscopy: Herzberg–Teller contributions," *The Journal of Chemical Physics*, vol. 84, no. 8, pp. 4174–4180, 1986.

[71] W. Ji, Y. Kitahama, X. Xue, B. Zhao, and Y. Ozaki, "Generation of pronounced resonance profile of charge-transfer contributions to surface-enhanced Raman scattering," *The Journal of Physical Chemistry C*, vol. 116, no. 3, pp. 2515–2520, 2012.

[72] L. Jensen, C. M. Aikens, and G. C. Schatz, "Electronic structure methods for studying surface-enhanced Raman scattering." *Chemical Society Reviews*, vol. 37, no. 5, pp. 1061–1073, 2008.

[73] C. H. Lin, L. Jiang, Y. H. Chai, H. Xiao, S. J. Chen, and H. L. Tsai, "One-step fabrication of nanostructures by femtosecond laser for surface-enhanced Raman scattering," *Optics Express*, vol. 17, no. 24, pp. 21 581–21 589, 2009.

[74] C. H. Lin, L. Jiang, H. Xiao, S. J. Chen, and H. L. Tsai, "Surface-enhanced Raman scattering microchip fabricated by femtosecond laser." *Optics Letters*, vol. 35, no. 17, pp. 2937–2939, 2010.

[75] P. Measor, L. Seballos, D. L. Yin, J. Z. Zhang, E. J. Lunt, A. R. Hawkins, and H. Schmidt, "On-chip surface-enhanced Raman scattering detection using integrated liquid-core waveguides," *Applied Physics Letters*, vol. 90, no. 21, p. 211107, 2007.

[76] P. R. Stoddart and D. J. White, "Optical fibre SERS sensors." *Analytical and Bioanalytical Chemistry*, vol. 394, no. 7, pp. 1761–1774, 2009.

[77] C. Viets, "Fibre-optic SERS sensors with angled tips," *Journal of Molecular Structure*, vol. 565-566, no. 1-3, pp. 515–518, 2001.

[78] D. J. White, A. P. Mazzolini, and P. R. Stoddart, "Fabrication of a range of SERS substrates on nanostructured multicore optical fibres," *Journal of Raman Spectroscopy*, vol. 38, no. 4, pp. 377–382, 2007.

[79] A. Dhawan, M. D. Gerhold, and J. F. Muth, "Plasmonic structures based on subwavelength apertures for chemical and biological sensing applications," *IEEE Sensors Journal*, vol. 8, no. 5-6, pp. 942–950, 2008.

[80] E. J. Smythe, M. D. Dickey, J. Bao, G. M. Whitesides, and F. Capasso, "Optical antenna arrays on a fiber facet for in situ surface-enhanced Raman scattering detection." *Nano Letters*, vol. 9, no. 3, pp. 1132–1138, 2009.

[81] X. Lan, Y. Han, T. Wei, Y. Zhang, L. Jiang, H. L. Tsai, and H. Xiao, "Surface-enhanced Raman-scattering fiber probe fabricated by femtosecond laser." *Optics Letters*, vol. 34, no. 15, pp. 2285–2287, 2009.

[82] A. Lucotti and G. Zerbi, "Fiber-optic SERS sensor with optimized geometry," *Sensors and Actuators B: Chemical*, vol. 121, no. 2, pp. 356–364, 2007.

[83] A. Pesapane, A. Lucotti, and G. Zerbi, "Fiber-optic SERS sensor with optimized geometry: testing and optimization," *Journal of Raman Spectroscopy*, vol. 41, no. 3, pp. 256–267, 2010.

[84] R. H. Clarke, S. Londhe, W. R. Premasiri, and M. E. Womble, "Low-resolution Raman spectroscopy: instrumentation and applications in chemical analysis," *Journal of Raman Spectroscopy*, vol. 30, no. 9, pp. 827–832, 1999.

[85] G. A. Lorigan, B. M. Patterson, A. J. Sommer, and N. D. Danielson, "Cost-effective spectroscopic instrumentation for the physical chemistry laboratory," *Journal of Chemical Education*, vol. 79, no. 10, pp. 1264–1266, 2002.

[86] M. A. Young, D. A. Stuart, O. Lyandres, M. R. Glucksberg, and R. P. Van Duyne, "Surface-enhanced Raman spectroscopy with a laser pointer light source and miniature," *Canadian Journal of Chemistry*, vol. 82, no. 10, pp. 1435–1441, 2004.

[87] P. Bisson, G. Parodi, D. Rigos, and J. E. Whitten, "Low-cost Raman spectroscopy using a violet diode laser," *The Chemical Educator*, vol. 11, no. 2, pp. 88–92, 2006.

[88] N. Hayazawa, Y. Inouye, Z. Sekkat, and S. Kawata, "Metallized tip amplification of near-field Raman scattering," *Optics Communications*, vol. 183, no. 1-4, pp. 333–336, 2000.

[89] J. Zhao, J. A. Dieringer, X. Y. Zhang, G. C. Schatz, and R. P. Van Duyne, "Wavelength-scanned surface-enhanced resonance Raman excitation spectroscopy," *The Journal of Physical Chemistry C*, vol. 112, no. 49, pp. 19 302–19 310, 2008.

[90] C. D. Geddes and J. R. Lakowicz, "Metal-enhanced fluorescence," *Journal of Fluorescence*, vol. 12, no. 2, pp. 121–129, 2002.

[91] E. Fort and S. Gresillon, "Surface enhanced fluorescence," *Journal of Physics D-Applied Physics*, vol. 41, no. 1, p. 013001, 2008.

[92] "Piranha Clean (Sulfuric Acid and Hydrogen Peroxide Mix)," *Standard Operating Procedure*, 2007.

[93] "http://www.menzel.de/Microscope_Slides.687.0.html?L=1."

[94] S. Honkanen, B. R. West, S. Yliniemi, P. Madasamy, M. Morrell, J. Auxier, A. Schulzgen, N. Peyghambarian, J. Carriere, J. Frantz, R. Kostuk, J. Castro, and D. Geraghty, "Recent advances in ion exchanged glass waveguides and devices," *Physics and Chemistry of Glasses-European Journal of Glass Science and Technology Part B*, vol. 47, no. 2, pp. 110–120, 2006.

[95] J. L. Jackel, "Glass waveguides made using low melting point nitrate mixtures," *Applied Optics*, vol. 27, no. 3, pp. 472–475, 1988.

[96] A. Tervonen, B. R. West, and S. Honkanen, "Ion-exchanged glass waveguide technology: a review," *Optical Engineering*, vol. 50, no. 7, p. 071107, 2011.

[97] X. Yang, M. Dubiel, S. Brunsch, and H. Hofmeister, "X-ray absorption spectroscopy analysis of formation and structure of Ag nanoparticles in soda-lime silicate glass," *Journal of Non-Crystalline Solids*, vol. 328, no. 1-3, pp. 123–136, 2003.

[98] X. Yang, W. Li, Z. Li, Y. Wei, and W. Huang, "Depth profiles of Ag nanoparticles in silicate glass," *Applied Physics A*, vol. 90, no. 3, pp. 465–467, 2007.

[99] J. P. Blondeau, F. Catan, C. Andreazza-Vigonlle, and N. Sbai, "Plasmon resonance and clustering of silver nanoclusters embedded in glass," *Plasmonics*, vol. 3, no. 2-3, pp. 65–71, 2008.

[100] M. Dubiel, J. Haug, H. Kruth, H. Hofmeister, and K. Schicke, "Ag/Na ion exchange in soda-lime glasses and the formation of small Ag nanoparticles," *Materials Science and Engineering: B*, vol. 149, no. 2, pp. 146–151, 2008.

[101] Y. Ma, J. A. Lin, S. A. Qin, N. Zhou, Q. Bian, H. Y. Wei, and Z. B. Feng, "Preparation of Ag nanocrystals embedded silicate glass by field-assisted diffusion and its properties of optical absorption," *Solid State Sciences*, vol. 12, no. 8, pp. 1413–1418, 2010.

[102] S. Yliniemi, Q. Wang, J. Albert, and S. Honkanen, "Studies on passive and active silver–sodium ion-exchanged glass waveguides and devices," *Materials Science and Engineering: B*, vol. 149, no. 2, pp. 152–158, 2008.

[103] X. Prieto-Blanco, "Electro-diffusion equations of monovalent cations in glass under charge neutrality approximation for optical waveguide fabrication," *Optical Materials*, vol. 31, no. 2, pp. 418–428, 2008.

[104] A. Quaranta, E. Cattaruzza, and F. Gonella, "Modelling the ion exchange process in glass: Phenomenological approaches and perspectives," *Materials Science and Engineering: B*, vol. 149, no. 2, pp. 133–139, 2008.

[105] R. G. Walker, C. D. W. Wilkinson, and J. A. H. Wilkinson, "Integrated optical waveguiding structures made by silver The propagation characteristics of stripe ion-exchanged waveguides ; a theoretical and experimental investigation," *Applied Optics*, vol. 22, no. 12, pp. 1923–1928, 1983.

[106] J. Z. Zou and R. T. Chen, "Improvement of two-step K^+-Na^+ and Ag^+-Na^+ ion-exchanged glass waveguides by surface removal," *Applied Physics Letters*, vol. 88, no. 8, 2006.

[107] Z. Rahman, S. Shukla, H. Cho, and S. Seal, "Tutorial : in-situ site-selective FIB for high resolution TEM sample preparation," *Microscopy and Analysis*, vol. 20, no. 3, pp. 9–11, 2006.

[108] G. De, M. Gusso, L. Tapfer, M. Catalano, F. Gonella, G. Mattei, P. Mazzoldi, and G. Battaglin, "Annealing behavior of silver, copper, and silver-copper nanoclusters in a silica matrix synthesized by the sol-gel technique," *Journal of Applied Physics*, vol. 80, no. 12, pp. 6734–6739, 1996.

[109] S. B. Donald, A. M. Swink, and H. D. Schreiber, "High-iron ferric glass," *Journal of Non-Crystalline Solids*, vol. 352, no. 6-7, pp. 539–543, 2006.

[110] K. Li, M. I. Stockman, and D. J. Bergman, "Self-similar chain of metal nanospheres as an efficient nanolens," *Physical Review Letters*, vol. 91, no. 22, pp. 1–4, 2003.

[111] E. C. Le Ru, E. Blackie, M. Meyer, and P. G. Etchegoin, "Surface enhanced Raman scattering enhancement factors: a comprehensive study," *The Journal of Physical Chemistry C*, vol. 111, no. 37, pp. 13 794–13 803, 2007.

[112] S. A. Asher, "UV resonance Raman studies of molecular structure and dynamics applications in physical and biophysical chemistry," *Annual Review of Physical Chemistry*, vol. 39, pp. 537–588, 1988.

[113] A. Merlen, V. Gadenne, J. Romann, V. Chevallier, L. Patrone, and J. C. Valmalette, "Surface enhanced Raman spectroscopy of organic molecules deposited on gold sputtered substrates." *Nanotechnology*, vol. 20, no. 21, p. 215705, 2009.

[114] N. Cade, T. Ritman-Meer, and D. Richards, "Plasmonic engineering of silver films for enhanced fluorescence and Raman scattering," *Proceeding of SPIE*, vol. 7192, p. 71920J, 2009.

[115] W. Zahn and A. Zösch, "Characterization of thin-film surfaces by fractal geometry," *Fresenius' Journal of Analytical Chemistry*, vol. 358, pp. 119–121, 1997.

[116] S. S. Wong, A. T. Woolley, T. W. Odom, J. L. Huang, P. Kim, D. V. Vezenov, and C. M. Lieber, "Single-walled carbon nanotube probes for high-resolution nanostructure imaging," *Applied Physics Letters*, vol. 73, no. 23, p. 3465, 1998.

[117] T. Larsen, K. Moloni, F. Flack, M. A. Eriksson, M. G. Lagally, and C. T. Black, "Comparison of wear characteristics of etched-silicon and carbon nanotube atomic-force microscopy probes," *Applied Physics Letters*, vol. 80, no. 11, p. 1996, 2002.

[118] M. Carmichael, R. Vidu, A. Maksumov, A. Palazoglu, and P. Stroeve, "Using wavelets to analyze AFM images of thin films: surface micelles and supported lipid bilayers," *Langmuir*, vol. 20, no. 26, pp. 11 557–11 568, 2004.

[119] H. R. Gutierrez, D. Nakabayashi, P. C. Silva, J. R. R. Bortoleto, V. Rodrigues, J. H. Clerici, M. A. Cotta, and D. Ugarte, "Carbon nanotube probe resolution: a quantitative analysis using Fourier Transform," *Physica Status Solidi (a)*, vol. 201, no. 5, pp. 888–893, 2004.

[120] N. R. Agarwal, E. Fazio, F. Neri, S. Trusso, C. Castiglioni, A. Lucotti, N. Santo, and P. M. Ossi, "Ag and Au nanoparticles for SERS substrates produced by pulsed laser ablation," *Crystal Research and Technology*, vol. 46, no. 8, pp. 836–840, 2011.

[121] J. Dong, J. Gong, J. Liu, M. Chen, and X. Yan, "The decoration of silver fractal-like nanostructure with Ag nanoparticles on the plastic slide for surface enhanced fluorescence," *Electrochimica Acta*, vol. 60, pp. 264–268, 2012.

Aalto-DD 125/2012

ISBN 978-952-60-4801-7
ISBN 978-952-60-4802-4 (pdf)
ISSN-L 1799-4934
ISSN 1799-4934
ISSN 1799-4942 (pdf)

Aalto University
School of Electrical Engineering
Department of Micro- and Nanosciences
www.aalto.fi

BUSINESS + ECONOMY

ART + DESIGN + ARCHITECTURE

SCIENCE + TECHNOLOGY

CROSSOVER

DOCTORAL DISSERTATIONS